Determining the impact of magma water contents on porphyry Cu fertility: constraints from hydrous and nominally anhydrous mineral analysis

WENTING HUANG[1, 2, 3], MICHAEL J. STOCK[2], XIAO-PING XIA [3,4*], XIAOMING SUN[5], ZEXIAN CUI[3,4], OUYANG LIUYUN[1,3], JIAN ZHANG[6], XILIAN CHEN[7], YI ZHENG[5], HUAYING LIANG[1,3*]

[1] Key Laboratory of Mineralogy and Metallogeny, Guangzhou Institute of Geochemistry, Chinese Academy of Sciences, Guangzhou 510640, China

[2] Department of Geology, Trinity College Dublin, Dublin, Ireland

[3]CAS Center for Excellence in Deep Earth Science, Guangzhou, 510640, China

[4]State Key Laboratory of Isotope Geochemistry, Guangzhou Institute of Geochemistry, Chinese Academy of Sciences, Guangzhou 510640, China

[5] Guangdong Provincial Key Lab of Geological Processes and Mineral Resource Survey, School of Earth Science and Engineering, Sun Yat-sen University, Guangzhou 510275, China

[6] Key Laboratory of Environment Change and Resources Use in Beibu Gulf, Ministry of Education, Nanning Normal University, Nanning 530001, China

[7] State Key Laboratory of Nuclear Resources and Environment, East China University of Technology, Nanchang 330013, China

* Corresponding authors, email: xpxia@gig.ac.cn (X.P. Xia), lianghy@gig.ac.cn (H.Y. Liang)

Abstract

Most large scale porphyry-style mineralization is genetically associated with oxidized, sulfur-rich and hydrous magmas, whose sources were enriched in mantle-derived or juvenile crustal-derived materials. Geochemical indices for these features can distinguish fertile magmas and barren magmas. However, fertile magmas which generate different sized porphyry deposits are usually geochemically indistinguishable and the factors controlling the size of porphyry mineralization are poorly understood. Here, we use zircon H_2O contents, and the compositions of apatite host in zircon, phenocrysts, and groundmass to compare the water contents and volatile evolution of fertile magmas in the Yulong ore belt, Tibet, which generated giant, large and medium sized porphyry deposits. We find that these porphyries have comparable major and trace element and zircon Hf-O isotope compositions, with high oxygen fugacity and sulfur contents. A negative correlation between $\frac{X_{Ap}^{Cl}}{X_{Ap}^{OH}}$ vs. $\frac{X_{Ap}^{F}}{X_{Ap}^{Cl}}$ of apatites suggests that the magmas consistently achieved H_2O saturation before zircon crystallization and zircon hydroxyl contents reveal that the melt water contents positively correlate with the size of the deposits, consistent with larger deposits achieving H_2O saturation at deeper crustal levels. The deeper H_2O saturation also caused the larger amount of Cl extraction, as indicated by the trends that $\frac{X_{Ap}^{F}}{X_{Ap}^{Cl}}$ increasing and the $\frac{X_{Ap}^{Cl}}{X_{Ap}^{OH}}$ decreasing with the deposit sizes. These datasets can be reconciled by magmas forming larger deposits having higher H_2O contents and suggest that the H_2O content is a key control on their fertility. Our study highlights the utility of integrated hydrous and nominally anhydrous mineral

analyses for constraining enigmatic magmatic volatile processes in magmatic ore-forming systems.

Introduction

Porphyry Cu deposits supply over 75% of the world's Cu production and are thought to form through the exsolution of metal-rich hydrothermal fluids from magmas at 5–15 km depth, which precipitate ores in the shallow (<6 km depth) crust (Hedenquist and Lowenstern, 1994; Richards, 2011b; Sillitoe, 2010). The ore-forming magmas are generally considered to be water-rich and formed in supra-subduction-zone and oceanic/continental arcs (Lu et al., 2015; Richards et al., 2012; Sillitoe, 2010; Wang et al., 2014; Wang et al., 2017). Measurement of magmatic water contents in porphyry-forming magmas has been hampered by lack of robust petrological volatile record in these systems: silicate melt inclusion and hydrous mineral volatile records are often compromised by (1) diffusive re-equilibration and (2) hydrothermal alteration (Bucholz et al., 2013; Gaetani et al., 2012; Portnyagin et al., 2008; Webster et al., 2017). However, hydrous mineral compositions (e.g. amphibole and biotite), whole-rock Sr/Y ratios, zircon Ti saturated temperatures and $(Eu_N/Eu^*) \times 10000/Y$ ratios have been successfully applied as proxies for the relative "wetness" (i.e. magmatic water concentration) of porphyry-forming magmas which has been identified as a discriminator between barren and fertile porphyry-forming magmas (Lu et al., 2015; Richards et al., 2012; Wang et al., 2014). These proxies are typically indistinguishable between magmas that formed small-scale mineralization and those that formed giant

deposits (Richards, 2013) and, as a result, the role of "wetness" in generating giant deposits remains controversial.

Previous studies have identified that water can occupy vacancies within the nominally anhydrous zircon lattice as hydroxyl ions (OH^-) in water-rich, SiO_2-saturated environment, and that the extent of zircon OH^- incorporation is related to the magmatic water activity (Botis et al., 2013; De Hoog et al., 2014; Nasdala et al., 2001a; Trail et al., 2010; Woodhead et al., 1991). As water diffusion in zircon is 1–2 orders of magnitude slower than in other magmatic minerals (e.g. olivine, garnet, and orthopyroxene; Zhang, 2015; Ingrin and Zhang, 2016), zircon crystals can preserve a record of magmatic water content/activity at the time of crystallization, without being reset by subsequent diffusional re-equilibration. In light of this, recent studies have shown that zircon water contents are a useful petrological tool for interrogating the magmatic water contents (Liebmann et al., 2021; Meng et al., 2021)

Volatile analysis in hydrous apatite [$Ca_5(PO_4)_3$(F, Cl, OH)] crystals has recently received increasing attention as a novel method for constraining the behavior and concentrations of magmatic volatiles in both terrestrial (Boyce and Hervig, 2008; Piccoli and Candela, 1994; Stock et al., 2016) and extra-terrestrial systems (Boyce et al., 2014; McCubbin et al., 2015). Recent studies have shown that phenocryst-hosted apatite inclusions preserve their volatile record at the time of entrapment and, given some knowledge about the order in which minerals crystallize, these can be used to

construct a relative chronology of volatile behavior in a magmatic system (Stock et al., 2018; Stock et al., 2016).

Here, we report the zircon water contents and the compositions of apatite inclusions host in zircon, phenocrysts, and groundmass from three fertile porphyry systems in the Yulong Cu belt (YCB here after), eastern Tibetan Plateau (Fig. 1), which formed medium-, large- and giant-size Cu deposits. We find systematic differences in hydrous (apatite) and nominally anhydrous (zircon) mineral compositions, which indicate systematic differences in magmatic volatile compositions at the time of zircon saturation, which correlate with the deposit size. Specifically, our data indicate that the size of these porphyry Cu deposits is impacted by the water concentration (i.e. "wetness") and mass of Cl extraction of the porphyry-forming magma.

Geological background and samples

The India-Asia collision at about 65-55 Ma has formed a series of fault systems in the eastern Tibetan Plateau (Peltzer and Tapponnier, 1988; Hou et al., 2003; Wang et al., 2020) and numerous potassic porphyry bodies occur along these faults (Fig. 1). Some of these porphyries were emplaced into the pull-apart basins along the northern Batang-Lijiang faults and generated giant- to medium-size porphyry Cu deposits which constitute the >100 km-long Yulong Cu belt (Campbell et al., 2014; Hou et al., 2003; Liang et al., 2006). These fertile intrusions have been dated at 36 to 41 Ma and share similar trace element and isotopic signatures (Campbell et al., 2014; Hou et al., 2003; Jiang et al., 2006; Liang et al., 2006).

106 We selected three fertile YCB porphyries (Fig. 2) for this study. These have
107 broadly comparable ages and geological associations, but extremely variable scales of
108 mineralization. They include: (1) the Yulong monzogranite porphyry (sample 83-271,
109 zircon U-Pb age: 40.9 Ma) which is associated with giant porphyry deposit with Cu
110 reserve > 6.5 Mt; (2) the Duoxiasongduo monzogranite porphyry (sample 83-388,
111 zircon U-Pb age: 37.5 Ma) which associated with a large porphyry deposit with Cu
112 reserve of ~1.0 Mt; and (3) the Zhanaga syenogranite porphyry (sample 83-432, zircon
113 U-Pb age: 38.5 Ma) which is associated with a medium deposit with Cu reserve of 0.65
114 Mt (Hou et al. 2003; Liang et al. 2006). These porphyries intruded into the Triassic
115 marine clastic and carbonate rocks are composed of multiphase intrusions and
116 underwent similar hydrothermal alteration including potassic silicate alteration, quartz-
117 sericite alteration, propylitic alteration and argillic to advanced alteration stage (Hou et
118 al., 2003).
119 The giant Yulong porphyry deposit is the largest deposit in the YCB. The porphyry
120 has a surface area of about 0.6 km^2 and is made up mainly of monzogranite porphyry
121 and quartz monzonite porphyry (Hou et al., 2003); mineralization occurs mainly in the
122 monzogranite porphyry. The Yulong deposit is composed of lenticular ore body hosted
123 in the porphyry and a stratiform ore body in the contact zone between the strata and the
124 porphyry. The size of the lenticular ore body is about 1000 m long, 600 m wide and
125 500 m deep. The stratiform ore body is ~200–300 m long, 130–200 m wide and ~20 –
126 100 m thick (Hou et al., 2003). For this study, we collected a sample of the syn-ore

127 monzogranite porphyry. This contains phenocrysts of plagioclase (10–15 vol.%), K-
128 feldspar (10–15 vol.%), biotite (5–10 vol.%), quartz (5–10 vol.%), and amphibole (3–
129 5 vol.%), with groundmass mainly consisting of K-feldspar (15–20 vol.%), quartz (25–
130 30 vol.%), plagioclase (15–20 vol.%) and biotite (3–5 vol.%; Fig. 2A). Accessory
131 phases include apatite, zircon, titanite and magnetite.

132 The large Duoxiasongduo porphyry deposit has a surface area of ~0.30 km^2 and is
133 the third largest deposit in the YCB. The porphyry consists mainly of alkaline feldspar
134 granite and monzogranite. The ore body is mainly hosted in the porphyry and is 600 m
135 long, 500 m wide and 570 m thick (Hou et al., 2003). For this study, we sampled the
136 syn-ore monzogranite porphyry, which contains phenocrysts of plagioclase (5–10
137 vol.%), K-feldspar (5–10 vol.%), quartz (5–10 vol.%), biotite (3–5 vol.%) and
138 amphibole (3–5 vol.%) with an aphanitic groundmass (Fig. 2B) and accessory zircon,
139 apatite, and magnetite.

140 The medium-sized Zhanaga porphyry deposit is close to the Yulong giant deposit
141 (Fig. 1B) and has a surface area of ~0.6 km^2. It consists of monzogranite and
142 syenogranite porphyry, which hosts veinlet/disseminated mineralization, with a ore
143 body ~540 m long, 200 m wide and 200 m thick (Hou et al. 2003). We sampled the syn-
144 ore syenogranite porphyry, which contains quartz (10-15 vol.%), plagioclase (5-10
145 vol.%), K-feldspar (5-10 vol.%), amphibole (5-10 vol.%), and biotite (5-10 vol.%)
146 phenocrysts set in a microcrystalline groundmass with similar mineral assemblage (Fig.
147 2C). Accessory phases include zircon, apatite, magnetite, and titanite.

Zircon occurs as a fine grained (~50–300 μm) groundmass phase in our samples. Cathodoluminescence imaging shows that zircon crystals from all three porphyries contain well-developed oscillatory zones zoning textures (Fig. 3A) and primary fluid inclusions (Fig. 3B). Apatite crystals are hosted within plagioclase (Fig. 4A), biotite (Fig. 4B), amphibole (Fig. 4C-D) and quartz (Fig. 4E-F) phenocrysts or occur in the groundmass (Fig. 4G-H). Some of the host-phenocrysts are cracked or altered (Fig. 4). We scanned the apatite crystals with electron microscope backscattered-electron (BSE) to reveal whether the crystals are altered. Scanning BSE images show that apatite crystals are either unzoned or oscillatory zoned. Some apatite crystals contain voids which have been are altered by hydrothermal fluids (Bouzari et al., 2016) were excluded from the analyses (Fig. 4); only the euhedral, inclusion-free grains were analyzed (Fig. 4F-H).

Methods

Sample preparation

Samples were prepared for analysis both as polished thin sections and grain mounts. Zircons from our three porphyry samples were separated from ~1 kg crushed rock using conventional heavy liquid and magnetic techniques before being mounted and polished for geochemical analysis. Phenocryst-hosted apatite inclusions and groundmass apatites were directly analyzed in thin sections, except for zircon-hosted apatites which were analysed in our epoxy zircon mounts. Transfer/reflected-light

micrography and cathodoluminescence (CL) imaging were performed before chemical analyses to reveal zircon internal textures and zircon-hosted apatite inclusions.

Whole-rock analysis.

Major element analysis. Two-hundred grams of each sample was crushed and sieved to 200 mesh after removing the weathered surface. For the major-element analyses, powered samples were mixed with $Li_2B_4O_7$ at a rate of 1:8 to make homogeneous glass disks by fusion at 1150-1200 ^oC. Glass discs were then analyzed by X-ray fluorescence spectroscopy (XRF) in the State Key Laboratory of Isotope Geochemistry (SKLIG), Guangzhou Institute of Geochemistry, Chinese Academy of Science (GIG-CAS) following procedures of Li et al., (2002). 2σ relative precision for XRF major element analyses is 1–3%, as determined by repeat analysis of appropriate secondary standards.

Trace element analysis. For the trace-elements analysis, the powered samples were dissolved in high-pressure Teflon bombs using HF + HNO_3 at 100^oC, following the procedures described by Liu et al. (1996). Solutions were then analysed using a Perkin-Elmer Sciex ELAN 6000 ionizing coupled plasma-mass spectrometer (ICP-MS) in the SKLIG, GIG-CAS, following procedures detailed by Li et al., (2006). A rhodium internal standard was used to monitor the signal drift and standards GSR-1 (GBW07103, China national certified reference materials), BHVO-1 (U.S. Geological Survey) and OU-6 (Potts and Kane, 2005) were used to calibrate elemental concentrations. 2σ relative precision for ICP-MS trace element analyses is <5% for

elements of ≥20 ppm and < 10% for elements <20 ppm, as determined by repeat analysis of appropriate secondary standards.

Zircon analyses

Zircon Raman spectroscopy. Zircon separates for Raman spectroscopy were mounted in epoxy before polishing. Only the zircon grains free of fluid inclusions and inherited cores in CL images were analysed. Analyses were conducted using a WITec alpha 300R high-resolution confocal Raman spectrometer at the KLMM, GIG-CAS, avoiding cracks or inclusions in the crystals. Raman spectra of were acquired by spot analysis, using the 532 nm laser, 300 mm^{-1} grating and a 50 × Zeiss objective, with 10 mW laser power, 5s acquisition time and 2.5 cm^{-1} resolution. Raman spectra were processed using the WITec Control Five software. Identification of Raman peaks was based on reference phase spectra from Frezzotti et al. (2012) and Rinaudo et al. (2003). The shift and the Full Width at Half Maximum (FWHM) of $\boldsymbol{\nu_3(SiO_4)}$ vibration band were measured after fitting to the Gaussian function.

Zircon water and oxygen isotope analyses. Zircon separates for secondary ion mass spectrometry (SIMS) were mounted in tin alloy before polishing to give low water backgrounds (<10 ppm; Zhang et al. 2018). Zircon H_2O concentration and oxygen isotope measurements were collected simultaneously using a CAMECA IMS 1280-HR SIMS spot analyses at the SKLIG, GIG-CAS, again avoiding inclusions or cracks in crystals. The samples were placed in the instrument high vacuum storage chamber overnight and further pumped down in the analysis chamber to $<2.0 \cdot 10^{-9}$ mbar prior

to analysis. The secondary ions were sputtered using a 3–5 nA Cs^+ source with 10 kV impact energy. ^{16}O and ^{18}O signals were detected by two Faraday cup detectors and $^{16}O^1H$ was simultaneously collected by an electron multiplier.

Each spot analysis lasted 4.5 minutes, including 200 s pre-sputter and secondary ion beam automatic centering, and ~1 minute to integrate 20 cycles of static $^{16}O^1H$, ^{16}O and ^{18}O measurement. The 2σ internal precision of $^{18}O/^{16}O$ and $^{16}O^1H/^{16}O$ are usually <0.4‰ and <0.5%, respectively. $^{18}O/^{16}O$ values were normalized to the Vienna Standard Mean Ocean Water standard (VSMOW: $^{18}O/^{16}O = 0.0020052$).

Zircon standards for H_2O contents were analyzed before and after the unknowns to establish a calibration curve for inversion of analytical $^{16}O^1H/^{16}O$ to H_2O concentration, following Xia et al. (2019). Using this method, H_2O detection limit has been determined to be ~10 ppm and the H_2O concentration 2σ precision is ~10% (Xia et al., 2019). The Penglai zircon standard was used to correct the instrument mass fractionation during oxygen isotope analysis and the Qinghu zircon was used as a secondary standard. The weighted mean $\delta^{18}O$ value obtained for the Qinghu zircon (5.54 ± 0.30‰, 2σ, n = 17) is within error of the recommended value (5.4 ± 0.2‰; Li et al. 2013).

Zircon Hf isotope analysis. Zircon Hf isotopes were analysed using a Neptune multicollector (MC)-ICP-MS coupled to a Resolution M-50 LA system at the SKLIG, GIG-CAS, following analytical and data reduction procedures described by Wu et al. (2005). Data were acquired using a 44 μm beam size at a 5 Hz repetition rate. Each

spot analysis lasted 70 s, with a 30 s blank collection (laser off) and 40 s signal detection (laser ablation). Measured isotope ratios of $^{176}Hf/^{177}Hf$ were normalized to $^{179}Hf/^{177}Hf = 0.7325$, using an exponential correction for mass bias. Repeat analysis of the Penglai zircon standard yielded $^{176}Hf/^{177}Hf = 0.282906 \pm 0.000036$ (2σ, n = 27), consistent with the recommended $^{176}Hf/^{177}Hf$ value of 0.282906 ± 0.000010 (2σ; Li et al. 2010).

The ^{176}Lu decay constant of $1.867\times10^{-11}a^{-1}$ (Söderlund et al., 2004) was used to calculate initial $^{176}Hf/^{177}Hf$. Present-day values for $^{176}Lu/^{177}Hf = 0.0336$ and $^{176}Hf/^{177}Hf = 0.282785$ of the chondritic uniform reservoir (Bouvier et al., 2008), and $^{176}Lu/^{177}Hf = 0.0384$ and $^{176}Hf/^{177}Hf = 0.284250$ of the depleted mantle (Griffin et al., 2000) were used in the calculation of the εHf values and the model ages.

Zircon trace element analysis. Zircon trace element concentrations (REE, U, Th, Hf, Y, Ti, P) were measured using a Thermo Fisher Scientific ELEMENT XR laser ablation-ionizing coupled- mass spectrometer (LA-ICP-MS), equipped with a 193-nm (ArF) Resonetics RESOlution M-50 laser system, at the SKLIG, GIG-CAS. Analysis were collected using 33 μm laser spots, with a constant 5 Hz repetition rate and a 4 J/cm^{-2} fluence, following analytical procedures were detailed by Zhang et al. (2019). NIST SRM 610 and 612 glass (Jochum et al., 2011; Pearce et al., 1997) and Temora zircon (Black et al., 2003) secondary standards were analyzed alongside unknows and 2σ relative precision is better than 8%.

Apatite major element analysis

Apatite major element concentrations were measured by electron microprobe analysis (EMPA), using a JEOL JXA-8230 instrument at the Key Laboratory of Mineralogy and Metallogeny, GIG-CAS. Analyses were collected using 15 kV accelerating voltage, 20 nA beam current, and 3–5 μm spot size. Fluorine and Cl were first analyzed and, where possible, apatite crystals were only selected for analysis where their c-axis was oriented perpendicular to the incident electron beam, to minimize halogen migration due to electron-beam-induced sample damage (Goldoff et al., 2012; Stock et al., 2015; Stormer et al., 1993).

Peak and background elemental counting times were 20s and 10s, respectively, for P, Ca, 10 s and 5 s for Cl, and F, 40 s and 20 s for Si, 60 s and 30 s for S. Calcium, P, and F were calibrated with Durango apatite, and Cl with tugtupite. Analytical accuracy is <1% for P, <2% for Ca and F, and <5% for Cl and S. Relative precision, quantified through repeated analyses of Wilberforce apatite, is ±2% for Ca, P, and F, and ± 4% for Cl. The apatite OH content was estimated by the difference, assuming a fully occupied Z site (Candela, 1986). The mole fraction of F, Cl and OH in apatite (X_F^{Ap}, X_{Cl}^{Ap} and X_{OH}^{Ap}) were calculated based on 25 oxygen.

Results

Whole-rock major and trace elements

The results of whole-rock geochemical analysis are reported in Table A1. Our porphyry samples from each of the three YCB deposits have similarly high SiO_2 (64.2–

69.2 wt.%) and alkali ($K_2O + Na_2O$ >8 wt.%, K_2O/Na_2O > 1.0; Fig. 5A) concentrations, high Al_2O_3 (13.7–17.1 wt.%), low TiO_2 (< 0.5 wt.%) and varying P_2O_5 contents (0.03–0.30 wt.%; Table A1). The samples plot into the quartz-monzonite field in a total alkali silica diagram (Fig. 5A) and the shoshonite field in a K_2O vs. SiO_2 diagram (Fig. 5B).

Our samples are highly enriched in large ion lithophile elements (K, Rb, Ba) and light rare earth elements but depleted in heavy rare earths and high-field strength elements (Fig. 6). They have listric-shape REE patterns with high chondrite-normalized $[La/Yb]_N$ ratios (21–50), Eu_N/Eu^* ranging 0.82–1.0 and Sr/Y ranging 19–86 (Table A1), showing arc-like and adakitic affinity (Richards et al., 2012).

Zircon Raman spectra

Raman spectra were collected for 45 zircon grains, with results (Raman shifts FWHM) reported in Table A2. Previous Raman spectroscopy studies revealed that the FWHM of the $\nu_3(SiO_4)$ band shows positive correlation with the degree of zircon radiation damage (Nasdala et al., 1995; Nasdala et al., 2001b) and, in our samples, the shift of the zircon $\nu_3(SiO_4)$ band is narrow (1004.0–1007.6 cm^{-1}; avg. 1006.1 ± 0.9 cm^{-1}). A representative baseline corrected Raman spectra for each Yulong deposit is shown in Figure A1, which is characterized by sharp peak (FWHMs = 3.3–7.3 cm^{-1}). Following Nasdala et al., (2001b) and Yang et al., (2022), these results indicate that zircon crystals are consistently primary (i.e. grew from their host porphyry magma) with negligible metamictization induced by radiation damage.

Zircon isotopic compositions

The O and Hf isotope compositions of zircons from the YCB are broadly comparable (Fig. 7; Tables A3 and A4): Zircons from Yulong, Duoxiasongduo and Zhanaga deposits each yield a narrow range of $\delta^{18}O$ values (6.6–7.6‰, 6.9–7.7‰ and 6.5–7.6 ‰, respectively) which overlap with one another (Fig. 7). These $\delta^{18}O$ ratios are consistently higher than average mantle value (5.3 ± 0.6‰; Valley et al. 1998).

Twenty zircon analyses from the Yulong deposit yielded $^{176}Hf/^{177}Hf$ in the range 0.282728–0.282936 and $\varepsilon_{Hf}(t)$ ranging -0.7–6.6 (calculated with U–Pb age of 40.9 Ma from Liang et al., 2006; Table A4). These have associated two-stage Hf model ages (T_{DM2}) of 691–1161 Ma. Nineteen zircon grains from Duoxiasongduo yielded $^{176}Hf/^{177}Hf$ ranging 0.282744–0.282899 and $\varepsilon_{Hf}(t)$ ranging –0.1–5.4 (calculated with U–Pb age of 37.5 Ma from Liang et al., 2006; Table A4), with associated T_{DM2} of 773–1122 Ma. Twenty-two zircon grains from the Zhanaga yielded $^{176}Hf/^{177}Hf$ ranging 0.282802–0.282927 and $\varepsilon_{Hf}(t)$ ranging 1.9–6.3 (calculated with U–Pb age of 38.5 Ma from Liang et al., 2006; Table A4), with associated T_{DM2} of 710–992 Ma.

Zircon trace element compositions

The trace element compositions of 59 zircons from the YCB are reported in Table A2. Zircons from each of our three studied porphyries have comparable U and Th concentrations, ranging 156–2211 ppm and 167–1343 ppm, respectively. These values indicate that the crystals received low α decay doses ($D\alpha < 3\times10^{15}$ events/mg), well

312 below the radiation damage threshold for point defects-dominated damage (Murakami
313 et al. 1991).

314 Despite having different absolute ∑REE and Y concentrations (Table A2), the
315 zircons from the three porphyries have similar chondrite-normalized (Fig. 8 and A2),
316 typical of igneous zircons with strong light rare earth element depletion and positive Ce
317 anomalies (Fig. 8 and A2). They also have high Eu_N/Eu^* (avg. 0.69) and trace element-
318 in-zircon oxybarometry returns a high oxygen fugacities (fO_2) which about two log
319 units above the quartz-fayalite-magnetite buffer (QFM, Table A2), consistent with
320 crystallization from highly oxidized magmas (Loucks, 2021). The mean $(Eu_N/Eu^*) \times$
321 $10000/Y$ ratio of our zircons is 9.9 ± 4.1(Table A2); this has been suggested as a proxy
322 for magma water content and is consistent with a 'wet' magma (Lu et al., 2016).

323 Incorporation of non-tetravalent cations into zircon structure (e.g. REEs and Y)
324 requires incorporation of other charge balancing ions to maintain stoichiometry,
325 through coupled substitutions. Most of our zircons have Fe <15 ppm, Mg <2 ppm and
326 Al <10 ppm but variable P concentrations ranging 28–277 ppm. ∑REE shows no
327 correlations with Mg, Fe or Al (Fig. A3 A-C) but a positive correlation with P (Fig. 9A-
328 B). This suggests that at least some of the REE and Y were incorporated by the
329 xenotime substitution (Finch et al., 2001):

330 $(REE+Y)^{3+} + P^{5+} = Zr^{4+} + Si^{4+}$ [1]

331 However, P/∑REE+Y ratios are consistently <<1.0, ranging 0.15–0.47 (avg. 0.25
332 ± 0.09) in the Yulong porphyry, 0.11–0.57 (avg. 0.26 ± 0.12) in the Duoxiasongduo

porphyry and 0.13–0.44 (avg. 0.22 ± 0.09) in the Zhanaga porphyry. These ratios indicate there was insufficient P^{5+} to fully charge-balance the REE^{3+} and Y^{3+} in the YCB zircons (Belousova et al., 2002; Hanchar and van Westrenen, 2007) and suggest that some charge compensation could be via a H-compensated trivalent substitution mechanism (De Hoog et al., 2014).

Zircon water contents and speciation

Water analyses of 59 zircon crystals from the YCB are in Table A3 (measured by SIMS). Zircons H_2O contents are highly variable in each individual sample, ranging from hundreds ppm to >1000 ppm, but show an overall positive correlation with the scale of mineralization in each deposit (Fig. 10A): zircon H_2O contents are typically highest in the giant Yulong porphyry deposit (n = 20; avg. 637 ± 233 ppm), have intermediate values in the large Duoxiasongduo porphyry (n = 17; avg. 574 ± 202 ppm), and are lowest in the medium Zhanaga porphyry (n = 22; avg. 319 ± 178 ppm). However, interpreting these data in the context of magmatic H_2O contents requires determination of the speciation and mechanism of H_2O incorporation in our zircon crystals.

Previous studies have identified two mechanisms of H_2O incorporation into non-metamict zircons (Botis et al., 2013; De Hoog et al., 2014; Nasdala et al., 2001a; Trail et al., 2010): first, H_2O can be incorporated as H^+ ions which are charge balanced by the coupled substitution of a trivalent anion in either the Zr site (De Hoog et al., 2014; Trail et al., 2010):

$$H^+ + (REE+Y)^{3+} = Zr^{4+} \quad [2]$$

or the Si site:

$Al^{3+} + H^{+} = Si^{4+}$ [3].

Second, H_2O can be incorporated as OH^- anions through a hydrogarnet-type substitution in the Si vacancy (Botis et al., 2013; De Hoog et al., 2014; Nasdala et al., 2001a; Trail et al., 2010):

$SiO_4 = (OH)_4$ [4]

or the Zr vacancy:

$ZrO_2 = (OH)_4$ [5]

Following eqs. 1 and 2, we estimate the maximum H^+ atomic concentrations in our crystals by subtracting the atomic concentration of P^{5+} from those of REE+Y^{3+} (Trail et al., 2010). As with H_2O_{total} (atomic concentration of H_2O), indicates that the H^+ concentrations are typically highest in the giant Yulong porphyry deposit (avg. 2.47 ± 1.06 apfu*1000), intermediate in the large Duoxiasongduo deposit (avg. 2.06 ± 0.68 apfu*1000) and lowest in the medium-sized Zhanaga deposit (avg. 1.57 ± 0.45 apfu*1000; Fig. 10B). However, the H_2O contents of our crystals far exceed those expected if H_2O incorporation was entirely through H^+ charge balancing for REE+Y^{3+} (Fig. 11C-D): if H_2O was entirely incorporated through this mechanism, (H_2O_{total}+P)/(REE+Y) would show a 1:1 correlation with REE+Y (De Hoog et al., 2014), but our samples consistently show elevated ratios (avg. 4.5 ± 1.7, n = 61; Fig. 9C-D). Calculated H^+/H_2O_{total} ratios are typically <0.2 (Fig. 11A), suggesting that H^+

374 substitution was not the dominant mechanism of H_2O uptake into our zircons and that
375 a significant quantity is incorporated as OH^-.

376 We estimate the minimum OH^- atomic contents of our zircons by subtracting
377 $REE+Y^{3+}$ from $H_2O_{total}+P^{5+}$ after Trail et al., (2010). In our samples, OH^-/H_2O_{total} ratios
378 are typically >0.8 (Fig. 11B), confirming that most H_2O is incorporated as OH^-, through
379 hydrogarnet-type substitution reactions (eqs. 4 and 5; Fig. 11C). As with total H_2O and
380 the H^+ concentration, OH^- concentrations correlate with the scale of mineralization in
381 the YCB deposits, with zircons from the giant Yulong porphyry typically having the
382 highest OH^- concentrations (avg. 11.7 ± 5.0 apfu*1000, n = 17), crystals from the large
383 Duoxiasongduo porphyry having intermediate concentrations (10.7 ± 4.2 apfu*1000, n
384 =22), and crystals from the medium Zhanaga porphyry having the lowest
385 concentrations (average at 5.5 ± 3.7 apfu*1000, n = 20; Fig. 10C).

386 ***Apatite volatile compositions***

387 The compositions of primary apatite crystals from the YCB are in Tables 1, A5
388 and Figures 12, 13. Crystals are sub-divided based on their textural association into: (1)
389 zircon-hosted apatite inclusions, (2) apatite inclusions within other phenocryst phases
390 (amphibole, biotite, plagioclase and quartz) and (3) groundmass apatite crystals.

391 Apatite inclusions hosted in plagioclase, biotite and quartz phenocrysts from the
392 giant Yulong porphyry deposit (n = 54) have similar compositions (Table 1), with low
393 Cl (0.03–0.18 wt.%), F (1.65–2.77 wt.%) and SO_3 (0.04–1.14 wt.%) contents (Fig. 12A,
394 E). Assuming stoichiometry, the low halogen contents imply that the crystals are

395 relatively OH-rich. The compositions of groundmass apatite crystals (n = 25; Cl = 0.04–
396 0.10 wt.%, F = 1.79–2.63 wt.%, and SO_3 = 0.08–0.48 wt.%) from the Yulong deposit
397 are comparable with those of phenocryst-hosted apatite (Fig. 12A). However, while
398 zircon-hosted apatite inclusions (n = 11) also have similar SO_3 content (0.08–0.71 wt.%)
399 (Fig. 12D), their halogen contents are distinctly variable (Cl = 0.08–0.33 wt.%, F =
400 1.26–2.53 wt.%) contents (Fig. 12A). Overall, apatites from the Yulong deposit
401 preserve negative $\frac{X_{Ap}^{F}}{X_{Ap}^{Cl}}$ vs. $\frac{X_{Ap}^{Cl}}{X_{Ap}^{OH}}$ correlations (Fig. 13A) and positive $\frac{X_{Ap}^{Cl}}{X_{Ap}^{OH}}$ vs. $\frac{X_{Ap}^{F}}{X_{Ap}^{OH}}$
402 correlations (Fig. A4A). These trends are consistent with water-saturated evolution
403 (either retaining their primary volatile compositions or later diffusive re-equilibration),
404 where Cl partitions preferentially (to F) into fluids, and fluid-melt partition coefficients
405 of F are >1 (Aiuppa et al., 2009; Baker and Alletti, 2012; Chevychelov et al., 2008;
406 Dolejš and Baker, 2007; Stock, 2016; Stock et al., 2018; Webster, 1990).
407 Apatite inclusions within amphibole, plagioclase, biotite and quartz phenocrysts
408 from the large Duoxiasongduo deposit have similar volatile composition (n = 82; Cl =
409 0.05–0.43 wt.%, F = 1.33–2.70 wt.%, SO_3 = 0.02–1.47 wt.%), which overlap with those
410 of groundmass crystals (n = 19; Cl = 0.08–0.24 wt.%, F = 1.60–2.79 wt.%, SO_3 = 0.20–
411 0.98 wt.%; Fig. 12B, E). The F (1.78–3.05 wt.%) and SO_3 (0.17–1.00 wt.%) contents
412 of zircon-hosted apatite inclusions are also similar but these crystals have distinctly
413 higher Cl contents (n = 16; 0.17–0.37 wt.%; Fig. 12B), which extend to higher values
414 (Fig. 12B). As in the Yulong deposit, $\frac{X_{Ap}^{F}}{X_{Ap}^{Cl}}$ ratios (9.13–73.3) in Duoxiasongduo apatites
415 show negative correlation with $\frac{X_{Ap}^{Cl}}{X_{Ap}^{OH}}$ (Fig. 13B) and positive correlation with $\frac{X_{Ap}^{F}}{X_{Ap}^{OH}}$

(0.50–3.18) (Fig. A4B), consistent with H_2O-saturated magmatic evolution (Stock et al. 2016, 2018; Stock, 2016). However, $\frac{X_{Ap}^{F}}{X_{Ap}^{Cl}}$ ratios are typically lower in Duoxiasongduo phenocryst-host and groundmass apatites comparing with those from the Yulong porphyry (Fig. 13E-F).

Apatite crystals from the medium-sized Zhanaga deposit exhibit some compositional differences to those from the Yulong and Duoxiasongduo porphyries (Table 1). Specifically, the Zhanaga apatites have similar volatile compositions regardless of their textural association (Table 1; Figs. 12C), with: 0.12–0.43 wt.% Cl, 1.58–2.44 wt.% F and 0.02–1.48 wt.% SO_3 in apatites hosted withing amphibole, biotite, plagioclase and quartz phenocrysts; 0.19–0.45 wt.% Cl, 1.56–2.60 wt.% F and 0.18–1.14 wt.% SO_3 in groundmass apatite crystals; and 0.19–0.48 wt.% Cl, 1.70–2.60 wt.% F and 0.15–1.12 wt.% SO_3 in zircon-hosted apatite inclusions. While Cl concentrations in the Zhanaga apatite crystals extend to higher values than in either of our other two porphyries (Fig. 12), their $\frac{X_{Ap}^{F}}{X_{Ap}^{Cl}}$ ratios are typically lower (<25, Fig. 13E-F). Zhanaga apatite crystals preserve the negative $\frac{X_{Ap}^{F}}{X_{Ap}^{Cl}}$ vs. $\frac{X_{Ap}^{Cl}}{X_{Ap}^{OH}}$ correlation (Fig. 13C) and positive $\frac{X_{Ap}^{Cl}}{X_{Ap}^{OH}}$ vs. $\frac{X_{Ap}^{F}}{X_{Ap}^{OH}}$ correlation (Fig. A4C), consistent with H_2O-saturated magmatic evolution (Stock et al. 2016, 2018; Stock, 2016).

Discussion

Petrogenetic fertility indicators in the YCB porphyries

Previous studies have identified several factors controlling the magma fertility for porphyry Cu deposits (Audétat et al., 2012; Chiaradia, 2020; Richards, 2013; Wilkinson,

2013). Compared to barren rocks, fertile magmas usually: (1) have magma sources comprising mantle-derived or juvenile crust-derived enriched material (Holwell et al., 2019; Hou et al., 2015; Richards, 2003; Richards, 2009); (2) are highly oxidized, promoting metal enrichment in the magma through delayed sulfide fractionation (Liang et al., 2009; Sillitoe, 2010; Sun et al., 2013), (3) are S-enriched generating mineralization with Cu/S ratios >100 (Gustafson and Hunt, 1975); and (4) have high H_2O contents, facilitating early H_2O saturation and the formation ore fluids, which extract metals from the magma, transport them to shallow crust and form porphyry deposits (Candela and Holland, 1986; Lu et al., 2015; Richards, 2011a; Wilkinson, 2013). However, while these features characterize most fertile magmas, to date, there is no evidence that they vary systematically between deposits of different sizes.

The giant Yulong, large Duoxiasongduo and medium Zhanaga porphyry deposits are related in space and time (Fig. 1). Their mineralized rocks have similar ages, share similar arc-like trace element patterns (Fig. 6A), indicating a shared tectonic background and petrogenesis. They also have similar zircon Hf-O isotope compositions (Fig. 7), with positive $\varepsilon_{Hf}(t)$ (avg. 2.85 ± 1.71) and $\delta^{18}O$ (avg. 6.91 ± 0.31) values, again attesting to a shared magma source, with melts likely derived from thickened juvenile mafic lower crust or delaminated lower crust (Hou et al., 2015; Hou et al., 2011)

The three fertile porphyries are all highly oxidized (avg. fO_2 = QFM+2), recorded by the high zircon Eu_N/Eu^* ratios (>0.4; Loader et al., 2017) and the presence of magnetite/hematite (Liang et al., 2009; Sun et al., 2013). Under these oxidized

conditions, sulfur in the melt generally occurs as S^{6+} (Jugo, 2009; Jugo et al., 2005) and enters apatite structure (Streck and Dilles, 1998). Our YCB apatites preserve high S contents (mean 0.43 wt.% SO_3), which are comparable to those in other fertile porphyries systems worldwide (SO_3 >0.5 wt.%; Streck and Dilles 1998; Chelle-Michou and Chiaradia 2017), indicating high sulfur contents in the oxidized magmas.

The abundance of hydrous minerals (e.g. amphibole, biotite) in our three porphyry systems attests to their high H_2O concentrations (Fig. 2). Similarly, high whole-rock Sr/Y (avg. 60 ± 18) and Eu_N/Eu^* ratios (avg. 0.88 ± 0.05), as well as the high zircon $(Eu_N/Eu^*) \times 10000/Y$ ratios (avg. 9.9 ± 4.1) are indicative of high magmatic H_2O contents (Loucks, 2021; Lu et al., 2015; Richards et al., 2012).

Overall, petrogenetic features of the Yulong, Duoxiasongduo and Zhanaga porphyry deposits (i.e. sources, high oxidation states, sulfur and H_2O-rich) are consistent with other 'fertile' porphyry systems worldwide, and elucidate the cluster of deposits in YCB. However, these established fertility indicators do not vary consistently between the giant, large and medium deposits and are therefore ineffective tools for differentiating deposit size.

Zircon water contents of different scale porphyry deposits

There are three major mechanisms for H_2O entering the crystal structure of zircon (Aines and Rossman, 1986; Botis et al., 2013; De Hoog et al., 2014; Nasdala et al., 2001a; Trail et al., 2010; Woodhead et al., 1991): (1) absorption into metamict zircons due to the accumulation of radiation damage through α-decay of U and Th (Aines and

Rossman, 1986; Woodhead et al., 1991); (2) entering the zircon structure in the form of H^+ through H-compensated trivalent substitution (reactions [2] and [3]) (De Hoog et al., 2014); and (3) hydrogarnet-type substitution in the form of OH^- (reactions [4] and [5]) (Botis et al., 2013; Nasdala et al., 2001a; Trail et al., 2010). In the first and second scenarios, zircon H_2O content do not record the water activity in their host magma (De Hoog et al., 2014). However, in the third scenario, H_2O content in zircon is mainly dependent on the water activity and pressure of the melt (Trail et al., 2010). In this case, we can theoretically compare the H_2O contents in the melts with similar compositions by comparing their zircon OH^- contents after excluding the influence of pressure. In H_2O-saturated condition, magmatic H_2O contents are equivalent to their H_2O solubility, as magmatic H_2O solubility is predominantly a function of pressure (Candela, 1986). Thus, the magmatic H_2O content and pressure would have uniform effect on the zircon OH^- content. This means that zircon OH^- content could serve as an indicator of both the magma water activity/content and magma storage depth (pressure) in H_2O-saturated conditions.

Our zircon samples are non-metamict and free of radiation damage, as indicated by their well-developed oscillatory zones (Fig. 3A), low radiation dose (D_{dpa} $<3\times10^{15}$ α-decay events/mg, calculated after Murakami et al. (1991)) and the FWHM of the $\nu_3(SiO_4)$ band being $<8cm^{-1}$ (Liebmann et al., 2021; Yang et al., 2022). This precludes H_2O absorption in our zircons.

While some H_2O is incorporated into our zircon crystals as H^+, where concentrations maybe affected by the REE^{3+} content in melt (De Hoog et al., 2014), most of the H_2O was incorporated through an OH^- substitution mechanism (Fig. 11). Primary fluid inclusions are common in our zircons (Fig. 4B) and directly attest that the ore-forming magmas had achieved H_2O saturation/exsolved fluids prior to the zircon crystallization. Moreover, apatite inclusions in our zircon crystals preserve the H_2O-saturated evolution trend (Fig. 13D), further supporting that the zircons have crystallized from a H_2O-saturated magma. Thus, the positive correlation between zircon OH^- concentration and the size of porphyry deposits in the YCB (Fig. 10C) reflects that the fertile magma of giant deposit having the highest water content during zircon crystallization. This correlation also demonstrates a fundamental connection between the depth of H_2O-saturation and the size of mineralization.

Deep fluid exsolution and the scale of porphyry-style mineralization

Apatites from the Yulong, Duoxiasongduo and Zhanaga porphyries consistently record H_2O-saturated magma evolution (Fig. 13, section 4.6). Since Cl partitions more strongly into magmatic fluids than F (Aiuppa et al., 2009; Alletti et al., 2009; Baker and Alletti, 2012; Webster et al., 2017), the apatites equilibrated with the earlier melts should have lower $\frac{X_{Ap}^{F}}{X_{Ap}^{Cl}}$ and higher $\frac{X_{Ap}^{Cl}}{X_{Ap}^{OH}}$ ratios than those equilibrated with later melts during the H_2O-saturated evolution (Stock et al., 2016; 2018).

Our amphibole, biotite, plagioclase, and quartz phenocrysts-hosted apatite inclusions have comparable volatile compositions to groundmass apatite crystals (Fig.

13A-C), suggesting that they do not preserve an earlier volatile record. As diffusive re-equilibration of apatite inclusions is very slow and unlikely to occur on normal magmatic timescale (Li et al., 2020; Stock et al., 2016), we interpret the phenocryst-hosted apatites have re-equilibrated with late-stage melts post-entrapment, as a result of their host-crystals being compromised by fracturing and/or alteration (Fig. 2; i.e. apatite inclusions are no longer "shielded" from the magma by their phenocryst host). In contrast, zircon-hosted apatite inclusions, especially those from the Yulong and Duoxiasongduo porphyries, have lower $\frac{X_{Ap}^{F}}{X_{Ap}^{Cl}}$ and higher $\frac{X_{Ap}^{Cl}}{X_{Ap}^{OH}}$ ratios than other apatite inclusions and groundmass apatite crystals (Fig. 13A-B), suggesting zircon-hosted apatite inclusions may preserve an earlier volatile record during their entrapment (i.e. refractory zircons are uncompromised host crystals).

However, regardless of the apatite textural association (zircon-hosted, phenocryst-hosted, or in groundmass), apatite $\frac{X_{Ap}^{F}}{X_{Ap}^{Cl}}$ is the highest in the giant Yulong porphyry deposit, and is the lowest in the medium-sized Zhanaga deposit (Fig. 13E-F), whereas the $\frac{X_{Ap}^{Cl}}{X_{Ap}^{OH}}$ ratios display the opposite trend (Fig. 13E-F; Fig. A4 E-F). The higher $\frac{X_{Ap}^{F}}{X_{Ap}^{Cl}}$ and the lower $\frac{X_{Ap}^{Cl}}{X_{Ap}^{OH}}$ values of apatite appear to link with greater extent of mineralization, possibly caused by different timing of volatile exsolution in the three porphyry systems.

Magmatic H_2O-saturated evolution would increase $\frac{X_{Ap}^{F}}{X_{Ap}^{Cl}}$ but decrease $\frac{X_{Ap}^{Cl}}{X_{Ap}^{OH}}$ ratios of apatite (Stock et al., 2016; 2018). As discussed above, the magmas generated giant/large porphyry deposits achieved H_2O-saturation at greater storage depths than that of the medium-sized deposit. The deeper magmatic H_2O-saturation would release

more fluid to interact with larger volume of melt, which promoted Cl extraction (Baker and Alletti, 2012; Hsu et al., 2019; Proffett, 2009; Wilkinson, 2013), and thereby drove apatite $\frac{X_{Ap}^{F}}{X_{Ap}^{Cl}}$ higher and $\frac{X_{Ap}^{Cl}}{X_{Ap}^{OH}}$ lower (cf. shallower H_2O-saturation). While Stock et al., (2016, 2018) typically envisage a slight positive correlation between $\frac{X_{Ap}^{F}}{X_{Ap}^{Cl}}$ and $\frac{X_{Ap}^{Cl}}{X_{Ap}^{OH}}$ during H_2O-saturated magmatic evolution, they consistently consider F to be incompatible in the fluid phase. We suggest that the slight negative correlation in our data (Fig. A4) maybe because F is, in fact, compatible in the Yulong porphyry fluids, consistent with recent experimental data (Aiuppa et al., 2009; Baker and Alletti, 2012; Chevychelov et al., 2008; Dolejš and Baker, 2007).

Crustal-derived magmas are usually F-rich but Cl-poor (Aiuppa et al., 2009; Liebmann et al., 2021), thus assimilation would likely increase apatite $\frac{X_{Ap}^{F}}{X_{Ap}^{Cl}}$ and decrease the $\frac{X_{Ap}^{Cl}}{X_{Ap}^{OH}}$. However, the Yulong porphyry has similar isotopic compositions to the other two porphyries (Fig. 7), indicating its highest $\frac{X_{Ap}^{F}}{X_{Ap}^{Cl}}$ and lowest $\frac{X_{Ap}^{Cl}}{X_{Ap}^{OH}}$ values are not caused by crustal assimilation.

Fractionation of volatile-bearing minerals (e.g., biotite, amphibole and apatite) may be expected to drive the decrease of both apatite $\frac{X_{Ap}^{F}}{X_{Ap}^{Cl}}$ and $\frac{X_{Ap}^{Cl}}{X_{Ap}^{OH}}$ ratios, because F typically partitions more strongly into common hydrous minerals (e.g., apatite, biotite, and amphibole) than Cl, and Cl more strongly than OH (Benard et al., 2017; Li and Hermann, 2017; Van den Bleeken and Koga, 2015). This is inconsistent with our data trends, thus fractionation of volatile-bearing minerals is unlikely the main mechanism.

We suggest that the relationship between higher $\frac{X_{Ap}^{F}}{X_{Ap}^{Cl}}$, lower $\frac{X_{Ap}^{Cl}}{X_{Ap}^{OH}}$ and the larger deposit sizes in YCB reflects the link between the mass of Cl extracted by volatile exsolution and the subsequent scale of mineralization. The magma generated the giant Yulong porphyry deposit achieved H_2O-saturation at deeper level, causing more Cl extraction than the large Duoxiasongduo porphyry deposit; while the saturation in the large Duoxiasongduo deposit was relatively deeper, and the Cl extraction was more than the medium-sized Zhanaga porphyry deposit (Fig. 14). This further demonstrates the relationship between the H_2O-saturation depth and the porphyry mineralization size. Since Cu and Mo formed Cl-complexes readily and partitioned into the fluid phase (Grondahl and Zajacz, 2017; Simon et al., 2006; Ulrich and Mavrogenes, 2008; Williams-Jones and Migdisov, 2014; Zajacz et al., 2011), deeper H_2O-saturation also likely caused more metal extraction, and hence higher potential to form larger porphyry mineralization.

Conclusions and implications for porphyry mineralization

Giant porphyry deposits are usually associated with more extensive hydrothermal alteration than smaller ones (Hou et al., 2003; Sillitoe, 2010). This indicates that giant ore-forming magmas have released more fluids and, theoretically, 'wetter' magmas should have higher potential to generate giant porphyry deposits. This correlation between magma wetness and porphyry mineralization intensity has been constrained by our study:

(1) Regardless of the deposit sizes, the three porphyries in YCB share similar sources and geochemical features, i.e., they are all comparable when considering established fertility indicators (high oxidation state, high sulfur content and water-rich). While these fertility indicators may effectively discriminate between baren and fertile systems, our data confirm that they do not correlate with the scale of porphyry mineralization.

(2) Magmas in each of our three porphyries were H_2O saturated at the time of zircon crystallization. The zircon OH^- content show a systematic increase with deposit size, indicating that the porphyry mineralization intensity correlates with the depth of H_2O-saturation.

(3) Apatite $\frac{X_{Ap}^{F}}{X_{Ap}^{Cl}}$ value show systematic increase with deposit size, whereas $\frac{X_{Ap}^{Cl}}{X_{Ap}^{OH}}$ shows an opposite trend. These trends reflect more Cl (and likely Cu and Mo) extraction in larger deposits due to deeper magmatic H_2O-saturation.

Since the depth of H_2O-saturation could be determined by the magma H_2O content, (2) and (3) further demonstrate the positive correlation between the magma H_2O content and the porphyry mineralization size.

Zircon H_2O contents and the apatite $\frac{X_{Ap}^{F}}{X_{Ap}^{Cl}}$ and $\frac{X_{Ap}^{Cl}}{X_{Ap}^{OH}}$ ratios could serve as indices of the relative magma wetness in other porphyry systems, where conventional petrological volatile indicators are less reliable (e.g. melt inclusions are crystallized). They could also be used as novel mineral-geochemical tools to assess the scale of porphyry mineralization potential.

Moreover, trace element studies in zircon-hosted apatite inclusion have been a topic of interest in detrital zircon provenance studies (e.g., Bruand et al., 2016; Meng et al., 2022; Jennings et al., 2011;). Our study highlights that the zircon-hosted apatite inclusions could preserve primary volatile compositions while the rest apatite has been re-equilibrated with the later-stage melt. Combination of trace elements and volatiles compositions of zircon-hosted apatite inclusions might also be relevant to determine the provenance in the search for ore deposits and in other applications.

Acknowledgments

This study was supported by the second Tibetan Plateau Scientific Expedition and Research (STEP; grant no. 2019QZKK0806), National Natural Science Foundation of China (42072088, 91855213), and the National Key R&D Program of China (2018YFA0702600). WH acknowledges the support from the China Scholarship Council (CSC) Scholarship (No. 202104910197). M.J. Stock was supported by a Frontiers for the Future grant (20/FFP-P/8895), co-funded by Science Foundation Ireland and Geological Survey Ireland. Elizabeth Bell and an anonymous reviewer are thanked for constructive comments and Reimar Seltmann for editorial handling. This is a contribution No. IS-3337 from GIGCAS.

References

Aines, R. D., and Rossman, G. R., 1986, Relationships between Radiation-Damage and Trace Water in Zircon, Quartz, and Topaz: American Mineralogist, v. 71, p. 1186-1193.

Aiuppa, A., Baker, D. R., and Webster, J. D., 2009, Halogens in volcanic systems:

624 Chemical Geology, v. 263, p. 1-18.
625 Alletti, M., Baker, D. R., Scaillet, B., Aiuppa, A., Moretti, R., and Ottolini, L.,
626 2009, Chlorine partitioning between a basaltic melt and H2O–CO2 fluids at Mount Etna:
627 Chemical Geology, v. 263, p. 37-50.
628 Audétat, A., Simon, A. C., Hedenquist, J. W., Harris, M., and Camus, F., 2012,
629 Magmatic Controls on Porphyry Copper Genesis, Geology and Genesis of Major
630 Copper Deposits and Districts of the World: A Tribute to Richard H. Sillitoe, 16, Society
631 of Economic Geologists, p. 0.
632 Baker, D. R., and Alletti, M., 2012, Fluid saturation and volatile partitioning
633 between melts and hydrous fluids in crustal magmatic systems: The contribution of
634 experimental measurements and solubility models: Earth-Science Reviews, v. 114, p.
635 298-324.
636 Belousova, E. A., Griffin, W. L., O'Reilly, S. Y., and Fisher, N. I., 2002, Igneous
637 zircon: trace element composition as an indicator of source rock type: Contributions to
638 Mineralogy and Petrology, v. 143, p. 602-622.
639 Benard, A., Koga, K. T., Shimizu, N., Kendrick, M. A., Ionov, D. A., Nebel, O.,
640 and Arculus, R. J., 2017, Chlorine and fluorine partition coefficients and abundances
641 in sub-arc mantle xenoliths (Kamchatka, Russia): Implications for melt generation and
642 volatile recycling processes in subduction zones: Geochimica Et Cosmochimica Acta,
643 v. 199, p. 324-350.
644 Black, L. P., Kamo, S. L., Allen, C. M., Aleinikoff, J. N., Davis, D. W., Korsch, R.
645 J., and Foudoulis, C., 2003, TEMORA 1: a new zircon standard for Phanerozoic U-
646 Pb geochronology: Chemical Geology, v. 200, p. 155-170.
647 Botis, S. M., Pan, Y. M., and Ewing, R. C., 2013, Hydrogen incorporation in
648 crystalline zircon: Insight from ab initio calculations: American Mineralogist, v. 98, p.
649 745-751.
650 Bouvier, A., Vervoort, J. D., and Patchett, P. J., 2008, The Lu–Hf and Sm–Nd
651 isotopic composition of CHUR: Constraints from unequilibrated chondrites and

652 implications for the bulk composition of terrestrial planets: Earth and Planetary Science
653 Letters, v. 273, p. 48-57.
654 Bouzari, F., Hart, C. J. R., Bissig, T., and Barker, S., 2016, Hydrothermal
655 Alteration Revealed by Apatite Luminescence and Chemistry: A Potential Indicator
656 Mineral for Exploring Covered Porphyry Copper Deposits: Economic Geology, v. 111,
657 p. 1397-1410.
658 Boyce, J. W., and Hervig, R. L., 2008, Magmatic degassing histories from apatite
659 volatile stratigraphy: Geology, v. 36, p. 63-66.
660 Boyce, J. W., Tomlinson, S. M., McCubbin, F. M., Greenwood, J. P., and
661 Treiman, A. H., 2014, The Lunar Apatite Paradox: Science, v. 344, p. 400-402.
662 Bruand, E., Storey, C., and Fowler, M., 2016, An apatite for progress: Inclusions
663 in zircon and titanite constrain petrogenesis and provenance: Geology, v. 44, no. 2, p.
664 91-94.
665 Bucholz, C. E., Gaetani, G. A., Behn, M. D., and Shimizu, N., 2013, Post-
666 entrapment modification of volatiles and oxygen fugacity in olivine-hosted melt
667 inclusions: Earth and Planetary Science Letters, v. 374, p. 145-155.
668 Campbell, I. H., Stepanov, A. S., Liang, H. Y., Allen, C. M., Norman, M. D., Zhang,
669 Y. Q., and Xie, Y. W., 2014, The origin of shoshonites: new insights from the Tertiary
670 high-potassium intrusions of eastern Tibet: Contributions to Mineralogy and Petrology,
671 v. 167.
672 Candela, P. A., 1986, Toward a Thermodynamic Model for the Halogens in
673 Magmatic Systems - an Application to Melt Vapor Apatite Equilibria: Chemical
674 Geology, v. 57, p. 289-301.
675 Candela, P. A., and Holland, H. D., 1986, A Mass-Transfer Model for Copper
676 and Molybdenum in Magmatic Hydrothermal Systems - the Origin of Porphyry-Type
677 Ore-Deposits: Economic Geology, v. 81, p. 1-19.
678 Chelle-Michou, C., and Chiaradia, M., 2017, Amphibole and apatite insights

679 into the evolution and mass balance of Cl and S in magmas associated with porphyry
680 copper deposits: Contributions to Mineralogy and Petrology, v. 172, p. 105.
681 Chevychelov, V. Y., Botcharnikov, R. E., and Hoitz, F., 2008, Partitioning of Cl
682 and F between fluid and hydrous phonolitic melt of Mt. Vesuvius at similar to 850-
683 1000 degrees C and 200 MPa: Chemical Geology, v. 256, p. 172-184.
684 Chiaradia, M., 2020, Gold endowments of porphyry deposits controlled by
685 precipitation efficiency: Nature Communications, v. 11, p. 248.
686 De Hoog, J. C. M., Lissenberg, C. J., Brooker, R. A., Hinton, R., Trail, D., and
687 Hellebrand, E., 2014, Hydrogen incorporation and charge balance in natural zircon:
688 Geochimica et Cosmochimica Acta, v. 141, p. 472-486.
689 Dolejš, D., and Baker, D. R., 2007, Liquidus Equilibria in the System K2O–
690 Na2O–Al2O3–SiO2–F2O−1–H2O to 100 MPa: II. Differentiation Paths of
691 Fluorosilicic Magmas in Hydrous Systems: Journal of Petrology, v. 48, p. 807-828.
692 Finch, R. J., Hanchar, J. M., Hoskin, P. W. O., and Burns, P. C., 2001, Rare-earth
693 elements in synthetic zircon: Part 2. A single-crystal X-ray study of xenotime
694 substitution: American Mineralogist, v. 86, p. 681-689.
695 Frezzotti, M. L., Tecce, F., and Casagli, A., 2012, Raman spectroscopy for fluid
696 inclusion analysis: Journal of Geochemical Exploration, v. 112, p. 1-20.
697 Gaetani, G. A., O'Leary, J. A., Shimizu, N., Bucholz, C. E., and Newville, M.,
698 2012, Rapid reequilibration of H2O and oxygen fugacity in olivine-hosted melt
699 inclusions: Geology, v. 40, p. 915-918.
700 Goldoff, B., Webster, J. D., and Harlov, D. E., 2012, Characterization of fluor-
701 chlorapatites by electron probe microanalysis with a focus on time-dependent intensity
702 variation of halogens: American Mineralogist, v. 97, p. 1103-1115.
703 Griffin, W. L., Pearson, N. J., Belousova, E., Jackson, S. E., van Achterbergh, E.,
704 O'Reilly, S. Y., and Shee, S. R., 2000, The Hf isotope composition of cratonic mantle:
705 LAM-MC-ICPMS analysis of zircon megacrysts in kimberlites: Geochimica Et

706 Cosmochimica Acta, v. 64, p. 133-147.
707 Grondahl, C., and Zajacz, Z., 2017, Magmatic controls on the genesis of
708 porphyry Cu–Mo–Au deposits: The Bingham Canyon example: Earth and Planetary
709 Science Letters, v. 480, p. 53-65.
710 Gustafson, L. B., and Hunt, J. P., 1975, The porphyry copper deposit at El
711 Salvador, Chile: Economic Geology, v. 70, p. 857-912.
712 Hanchar, J. M., and van Westrenen, W., 2007, Rare earth element behavior in
713 zircon-melt systems: Elements, v. 3, p. 37-42.
714 Hedenquist, J. W., and Lowenstern, J. B., 1994, The Role of Magmas in the
715 Formation of Hydrothermal Ore-Deposits: Nature, v. 370, p. 519-527.
716 Holwell, D. A., Fiorentini, M., McDonald, I., Lu, Y., Giuliani, A., Smith, D. J.,
717 Keith, M., and Locmelis, M., 2019, A metasomatized lithospheric mantle control on
718 the metallogenic signature of post-subduction magmatism: Nature Communications, v.
719 10, p. 3511.
720 Hou, Z., Yang, Z., Lu, Y., Kemp, A., Zheng, Y., Li, Q., Tang, J., Yang, Z., and
721 Duan, L., 2015, A genetic linkage between subduction- and collision-related porphyry
722 Cu deposits in continental collision zones: Geology, v. 43, p. 247-250.
723 Hou, Z., Zhang, H., Pan, X., and Yang, Z., 2011, Porphyry Cu (–Mo–Au)
724 deposits related to melting of thickened mafic lower crust: Examples from the eastern
725 Tethyan metallogenic domain: Ore Geology Reviews, v. 39, p. 21-45.
726 Hou, Z. Q., Ma, H. W., Zaw, K., Zhang, Y. Q., Wang, M. J., Wang, Z., Pan, G. T.,
727 and Tang, R. L., 2003, The Himalayan Yulong porphyry copper belt: Product of large-
728 scale strike-slip faulting in eastern Tibet: Economic Geology and the Bulletin of the
729 Society of Economic Geologists, v. 98, p. 125-145.
730 Hsu, Y.-J., Zajacz, Z., Ulmer, P., and Heinrich, C. A., 2019, Chlorine partitioning
731 between granitic melt and H2O-CO2-NaCl fluids in the Earth's upper crust and
732 implications for magmatic-hydrothermal ore genesis: Geochimica et Cosmochimica
733 Acta, v. 261, p. 171-190.

Ingrin, J., and Zhang, P.P. 2016, Hydrogen diffusion in Zircon. EGU General Assembly Conference 2016., 18.

Jiang, Y.-H., Jiang, S.-Y., Ling, H.-F., and Dai, B.-Z., 2006, Low-degree melting of a metasomatized lithospheric mantle for the origin of Cenozoic Yulong monzogranite-porphyry, east Tibet: Geochemical and Sr–Nd–Pb–Hf isotopic constraints: Earth and Planetary Science Letters, v. 241, p. 617-633.

Jennings, E. S., Marschall, H. R., Hawkesworth, C. J., and Storey, C. D., 2011, Characterization of magma from inclusions in zircon: Apatite and biotite work well, feldspar less so: Geology, v. 39, no. 9, p. 863-866.

Jochum, K. P., Weis, U., Stoll, B., Kuzmin, D., Yang, Q. C., Raczek, I., Jacob, D. E., Stracke, A., Birbaum, K., Frick, D. A., Gunther, D., and Enzweiler, J., 2011, Determination of Reference Values for NIST SRM 610-617 Glasses Following ISO Guidelines: Geostandards and Geoanalytical Research, v. 35, p. 397-429.

Jugo, P. J., 2009, Sulfur content at sulfide saturation in oxidized magmas: Geology, v. 37, p. 415-418.

Jugo, P. J., Luth, R. W., and Richards, J. P., 2005, Experimental data on the speciation of sulfur as a function of oxygen fugacity in basaltic melts: Geochimica Et Cosmochimica Acta, v. 69, p. 497-503.

Li, H. J., and Hermann, J., 2017, Chlorine and fluorine partitioning between apatite and sediment melt at 2.5 GPa, 800 degrees C: A new experimentally derived thermodynamic model: American Mineralogist, v. 102, p. 580-594.

Li, J.-X., Li, G.-M., Evans, N. J., Zhao, J.-X., Qin, K.-Z., and Xie, J., 2021, Primary fluid exsolution in porphyry copper systems: evidence from magmatic apatite and anhydrite inclusions in zircon: Mineralium Deposita, v. 56, p. 407-415.

Li, W., Chakraborty, S., Nagashima, K., and Costa, F., 2020, Multicomponent diffusion of F, Cl and OH in apatite with application to magma ascent rates: Earth and Planetary Science Letters, v. 550, p. 116545.

761 Li, X.-H., Li, Z.-X., Wingate, M. T. D., Chung, S.-L., Liu, Y., Lin, G.-C., and Li,
762 W.-X., 2006, Geochemistry of the 755Ma Mundine Well dyke swarm, northwestern
763 Australia: Part of a Neoproterozoic mantle superplume beneath Rodinia?: Precambrian
764 Research, v. 146, p. 1-15.
765 Li, X.-h., Li, Z.-X., Zhou, H., Liu, Y., and Kinny, P. D., 2002, U–Pb zircon
766 geochronology, geochemistry and Nd isotopic study of Neoproterozoic bimodal
767 volcanic rocks in the Kangdian Rift of South China: implications for the initial rifting
768 of Rodinia: Precambrian Research, v. 113, p. 135-154.
769 Li, X.-H., Long, W.-G., Li, Q.-L., Liu, Y., Zheng, Y.-F., Yang, Y.-H., Chamberlain,
770 K. R., Wan, D.-F., Guo, C.-H., Wang, X.-C., and Tao, H., 2010, Penglai Zircon
771 Megacrysts: A Potential New Working Reference Material for Microbeam
772 Determination of Hf–O Isotopes and U–Pb Age: Geostandards and Geoanalytical
773 Research, v. 34, p. 117-134.
774 Li, X., Tang, G., Gong, B., Yang, Y., Hou, K., Hu, Z., Li, Q., Liu, Y., and Li, W.,
775 2013, Qinghu zircon: A working reference for microbeam analysis of U-Pb age and Hf
776 and O isotopes: Chinese Science Bulletin, v. 58, p. 4647-4654.
777 Liang, H. Y., Campbell, I. H., Allen, C., Sun, W. D., Liu, C. Q., Yu, H. X., Xie, Y.
778 W., and Zhang, Y. Q., 2006, Zircon Ce4+/Ce3+ ratios and ages for Yulong ore-bearing
779 porphyries in eastern Tibet: Mineralium Deposita, v. 41, p. 152-159.
780 Liang, H. Y., Sun, W. D., Ling, M. X., Ding, X., and Yang, X., 2009, Porphyry
781 Cu (Au) deposit promoted by redox decoupling during magnetite alteration in Yulong:
782 Geochimica Et Cosmochimica Acta, v. 73, p. A761-A761.
783 Liebmann, J., Spencer, C. J., Kirkland, C. L., Xia, X. P., and Bourdet, J., 2021,
784 Effect of water on delta O-18 in zircon: Chemical Geology, v. 574.
785 Liu, Y., Liu, H. C., and Li, X. H., 1996, Simultaneous and precise determination
786 of 40 trace elements in rock samples using ICP-MS: Geochimica v. 25, p. 552-558.
787 Loader, M. A., Wilkinson, J. J., and Armstrong, R. N., 2017, The effect of titanite
788 crystallisation on Eu and Ce anomalies in zircon and its implications for the assessment

789 of porphyry Cu deposit fertility: Earth and Planetary Science Letters, v. 472, p. 107-
790 119.
791 Loucks, R. R., 2021, Deep entrapment of buoyant magmas by orogenic tectonic
792 stress: Its role in producing continental crust, adakites, and porphyry copper deposits:
793 Earth-Science Reviews, v. 220, p. 103744.
794 Lu, Y.-J., Loucks, R. R., Fiorentini, M., McCuaig, T. C., Evans, N. J., Yang, Z.-M.,
795 Hou, Z.-Q., Kirkland, C. L., Parra-Avila, L. A., Kobussen, A., and Richards, J. P.,
796 2016, Zircon Compositions as a Pathfinder for Porphyry Cu ± Mo ± Au Deposits,
797 Tectonics and Metallogeny of the Tethyan Orogenic Belt, 19, Society of Economic
798 Geologists, p. 0.
799 Lu, Y. J., Loucks, R. R., Fiorentini, M. L., Yang, Z. M., and Hou, Z. Q., 2015,
800 Fluid flux melting generated postcollisional high Sr/Y copper ore-forming water-rich
801 magmas in Tibet: Geology, v. 43, p. 583-586.
802 McCubbin, F. M., Vander Kaaden, K. E., Tartese, R., Boyce, J. W., Mikhail, S.,
803 Whitson, E. S., Bell, A. S., Anand, M., Franchi, I. A., Wang, J. H., and Hauri, E. H.,
804 2015, Experimental investigation of F, Cl, and OH partitioning between apatite and Fe-
805 rich basaltic melt at 1.0-1.2 GPa and 950-1000 degrees C: American Mineralogist, v.
806 100, p. 1790-1802.
807 Meng, J. T., Xia, X. P., Ma, L., Jiang, Z. Q., Xu, J., Cui, Z. X., Yang, Q., Zhang,
808 W. F., and Zhang, L., 2021, A H2O-in-zircon perspective on the heterogeneous water
809 content of crust-derived magmas in southern Tibet: Science China-Earth Sciences.
810 Meng, X., Simon, A. C., Kleinsasser, J. M., Mole, D. R., Kontak, D. J., Jugo, P.
811 J., Mao, J., and Richards, J. P., 2022, Formation of oxidized sulfur-rich magmas in
812 Neoarchaean subduction zones: Nature Geoscience, v. 15, no. 12, p. 1064-1070.
813 Murakami, T., B. C. Chakoumakos, R. C. Ewing, G. R. Lumpkin, and W. J. Weber,
814 1991, Alpha-Decay Event Damage in Zircon. American Mineralogist, 76, 1510-1532.
815 Nasdala, L., Beran, A., Libowitzky, E., and Wolf, D., 2001a, The incorporation

816 of hydroxyl groups and molecular water in natural zircon (ZrSiO4): American Journal
817 of Science, v. 301, p. 831-857.
818 Nasdala, L., Irmer, G., and Wolf, D., 1995, The Degree of Metamictization in
819 Zircon - a Raman-Spectroscopic Study: European Journal of Mineralogy, v. 7, p. 471-
820 478.
821 Nasdala, L., Wenzel, M., Vavra, G., Irmer, G., Wenzel, T., and Kober, B., 2001b,
822 Metamictisation of natural zircon: accumulation versus thermal annealing of
823 radioactivity-induced damage: Contributions to Mineralogy and Petrology, v. 141, p.
824 125-144.
825 Pearce, N. J. G., Perkins, W. T., Westgate, J. A., Gorton, M. P., Jackson, S. E., Neal,
826 C. R., and Chenery, S. P., 1997, A compilation of new and published major and trace
827 element data for NIST SRM 610 and NIST SRM 612 glass reference materials:
828 Geostandards Newsletter-the Journal of Geostandards and Geoanalysis, v. 21, p. 115-
829 144.
830 Peltzer, G., and Tapponnier, P., 1988, Formation and Evolution of Strike-Slip
831 Faults, Rifts, and Basins during the India-Asia Collision - an Experimental Approach:
832 Journal of Geophysical Research-Solid Earth and Planets, v. 93, p. 15085-&.
833 Piccoli, P., and Candela, P., 1994, Apatite in felsic rocks; a model for the
834 estimation of initial halogen concentrations in the Bishop Tuff (Long Valley) and
835 Tuolumne Intrusive Suite (Sierra Nevada Batholith) magmas: American Journal of
836 Science, v. 294, p. 92-135.
837 Portnyagin, M., Almeev, R., Matveev, S., and Holtz, F., 2008, Experimental
838 evidence for rapid water exchange between melt inclusions in olivine and host magma:
839 Earth and Planetary Science Letters, v. 272, p. 541-552.
840 Potts, P. J., and Kane, J. S., 2005, International Association of Geoanalysts
841 Certificate of Analysis: Certified Reference Material OU-6 (Penrhyn Slate):
842 Geostandards and Geoanalytical Research, v. 29, p. 233-236.
843 Proffett, J. M., 2009, High Cu grades in porphyry Cu deposits and their

relationship to emplacement depth of magmatic sources: Geology, v. 37, p. 675-678.

Richards, J. P., 2003, Tectono-Magmatic Precursors for Porphyry Cu-(Mo-Au) Deposit Formation: Economic Geology, v. 98, p. 1515-1533.

Richards, J. P., 2009, Postsubduction porphyry Cu-Au and epithermal Au deposits: Products of remelting of subduction-modified lithosphere: Geology, v. 37, p. 247-250.

Richards, J. P., 2011a, HIGH Sr/Y ARC MAGMAS AND PORPHYRY Cu +/- Mo +/- Au DEPOSITS: JUST ADD WATER: Economic Geology, v. 106, p. 1075-1081.

Richards, J. P., 2011b, Magmatic to hydrothermal metal fluxes in convergent and collided margins: Ore Geology Reviews, v. 40, p. 1-26.

Richards, J. P., 2013, Giant ore deposits formed by optimal alignments and combinations of geological processes: Nature Geoscience, v. 6, p. 911-916.

Richards, J. P., Spell, T., Rameh, E., Razique, A., and Fletcher, T., 2012, High Sr/Y Magmas Reflect Arc Maturity, High Magmatic Water Content, and Porphyry Cu +/- Mo +/- Au Potential: Examples from the Tethyan Arcs of Central and Eastern Iran and Western Pakistan: Economic Geology, v. 107, p. 295-332.

Rinaudo, C., Gastaldi, D., and Belluso, E., 2003, Characterization of chrysotile, antigorite and lizardite by FT-Raman spectroscopy: Canadian Mineralogist, v. 41, p. 883-890.

Sillitoe, R. H., 2010, Porphyry Copper Systems: Economic Geology, v. 105, p. 3-41.

Simon, A. C., Pettke, T., Candela, P. A., Piccoli, P. M., and Heinrich, C. A., 2006, Copper partitioning in a melt-vapor-brine-magnetite-pyrrhotite assemblage: Geochimica Et Cosmochimica Acta, v. 70, p. 5583-5600.

Söderlund, U., Patchett, P. J., Vervoort, J. D., and Isachsen, C. E., 2004, The 176Lu decay constant determined by Lu–Hf and U–Pb isotope systematics of Precambrian mafic intrusions: Earth and Planetary Science Letters, v. 219, p. 311-324.

Stock, M. J., 2016, The volatile history of past volcanic eruptions. PhD thesis, University of Oxford.

Stock, M. J., Humphreys, M. C. S., Smith, V. C., Isaia, R., Brooker, R. A., and Pyle, D. M., 2018, Tracking Volatile Behaviour in Sub-volcanic Plumbing Systems Using Apatite and Glass: Insights into Pre-eruptive Processes at Campi Flegrei, Italy: Journal of Petrology, v. 59, p. 2463-2491.

Stock, M. J., Humphreys, M. C. S., Smith, V. C., Isaia, R., and Pyle, D. M., 2016, Late-stage volatile saturation as a potential trigger for explosive volcanic eruptions: Nature Geoscience, v. 9, p. 249-254.

Stock, M. J., Humphreys, M. C. S., Smith, V. C., Johnson, R. D., Pyle, D. M., and EIMF, 2015, New constraints on electron-beam induced halogen migration in apatite†: American Mineralogist, v. 100, p. 281-293.

Stormer, J. C., Pierson, M. L., and Tacker, R. C., 1993, Variation of F and Cl X-ray intensity due to anisotropic diffusion in apatite during electron microprobe analysis: American Mineralogist, v. 78, p. 641-648.

Streck, M. J., and Dilles, J. H., 1998, Sulfur evolution of oxidized arc magmas as recorded in apatite from a porphyry copper batholith: Geology, v. 26, p. 523-526.

Sun, W.-d., Liang, H.-y., Ling, M.-x., Zhan, M.-z., Ding, X., Zhang, H., Yang, X.-y., Li, Y.-l., Ireland, T. R., Wei, Q.-r., and Fan, W.-m., 2013, The link between reduced porphyry copper deposits and oxidized magmas: Geochimica et Cosmochimica Acta, v. 103, p. 263-275.

Sun, and McDonough, 1989, Chemical and isotopic systematics of oceanic basalts: Implications for mantle composition and processes. Geological Society London Special Publications, 42.

Trail, D., Thomas, J. B., and Watson, E. B., 2010, The incorporation of hydroxyl into zircon: American Mineralogist, v. 96, p. 60-67.

Ulrich, T., and Mavrogenes, J., 2008, An experimental study of the solubility of molybdenum in H2O and KCl-H2O solutions from 500°C to 800°C and 150 to 300 MPa: Geochimica et Cosmochimica Acta, v. 72, p. 2316−2330.

Valley, J. W., Kinny, P. D., Schulze, D. J., and Spicuzza, M. J., 1998, Zircon

megacrysts from kimberlite: oxygen isotope variability among mantle melts: Contributions to Mineralogy and Petrology, v. 133, p. 1-11.

Van den Bleeken, G., and Koga, K. T., 2015, Experimentally determined distribution of fluorine and chlorine upon hydrous slab melting, and implications for F-Cl cycling through subduction zones: Geochimica Et Cosmochimica Acta, v. 171, p. 353-373.

Wang, R., Richards, J. P., Hou, Z. Q., Yang, Z. M., and DuFrane, S. A., 2014, Increased Magmatic Water Content-The Key to Oligo-Miocene Porphyry Cu-Mo +/-Au Formation in the Eastern Gangdese Belt, Tibet: Economic Geology, v. 109, p. 1315-1339.

Wang, R., Tafti, R., Hou, Z. Q., Shen, Z. C., Guo, N., Evans, N. J., Jeon, H., Li, Q. Y., and Li, W. K., 2017, Across-arc geochemical variation in the Jurassic magmatic zone, Southern Tibet: Implication for continental arc-related porphyry Cu-Au mineralization: Chemical Geology, v. 451, p. 116-134.

Wang, R., Zhu, D.C., Wang, Q., Hou, Z.Q., Yang, Z.M., Zhao, Z.D. and Mo, X.X., 2020, Porphyry mineralization in the Tethyan orogen: Science China Earth Sciences, v. 63, p. 2029–2041.

Webster, J. D., 1990, Partitioning of F between H2O and CO2 fluids and topaz rhyolite melt: Contributions to Mineralogy and Petrology, v. 104, p. 424-438.

Webster, J. D., Goldoff, B. A., Flesch, R. N., Nadeau, P. A., and Silbert, Z. W., 2017, Hydroxyl, Cl, and F partitioning between high-silica rhyolitic melts-apatite-fluid(s) at 50-200 MPa and 700-1000 degrees C: American Mineralogist, v. 102, p. 61-74.

Wilkinson, J. J., 2013, Triggers for the formation of porphyry ore deposits in magmatic arcs: Nature Geoscience, v. 6, p. 917-925.

Williams-Jones, A. E., and Migdisov, A. A., 2014, Experimental Constraints on the Transport and Deposition of Metals in Ore-Forming Hydrothermal Systems: Building Exploration Capability for the 21st Century, p. 77-95.

928 Woodhead, J. A., Rossman, G. R., and Thomas, A. P., 1991, Hydrous Species in
929 Zircon: American Mineralogist, v. 76, p. 1533-1546.
930 Wu, F.-Y., Yang, J.-H., Wilde, S. A., and Zhang, X.-O., 2005, Geochronology,
931 petrogenesis and tectonic implications of Jurassic granites in the Liaodong Peninsula,
932 NE China: Chemical Geology, v. 221, p. 127-156.
933 Xia, X. P., Cui, Z. X., Li, W. C., Zhang, W. F., Yang, Q., Hui, H. J., and Lai, C.
934 K., 2019, Zircon water content: reference material development and simultaneous
935 measurement of oxygen isotopes by SIMS: Journal of Analytical Atomic Spectrometry,
936 v. 34, p. 1088-1097.
937 Yang, C.-M., Xu, Y.-G., Xia, X.-P., Gao, Y.-Y., Zhang, W.-F., Yang, Y.-N., Yang,
938 Q., and Zhang, L., 2022, Raman spectroscopy-based screening of zircon for reliable
939 water content and oxygen isotope measurements: American Mineralogist, v. 107, p.
940 936-945.
941 Zajacz, Z., Seo, J. H., Candela, P. A., Piccoli, P. M., and Tossell, J. A., 2011, The
942 solubility of copper in high-temperature magmatic vapors: A quest for the significance
943 of various chloride and sulfide complexes: Geochimica et Cosmochimica Acta, v. 75,
944 p. 2811-2827.
945 Zhang, L., Ren, Z. Y., Xia, X. P., Yang, Q., Hong, L. B., and Wu, D., 2019, In
946 situ determination of trace elements in melt inclusions using laser ablation inductively
947 coupled plasma sector field mass spectrometry: Rapid Communications in Mass
948 Spectrometry, v. 33, p. 361-370.
949 Zhang, W. F., Xia, X. P., Zhang, Y. Q., Peng, T. P., and Yang, Q., 2018, A novel
950 sample preparation method for ultra-high vacuum (UHV) secondary ion mass
951 spectrometry (SIMS) analysis: Journal of Analytical Atomic Spectrometry, v. 33.
952 Zhang, P.P. 2015, Hydrogen diffusion in NAMs: andradite garnet and zircon. Ph.D.
953 thesis, Université de Lille.

954 **Figure Captions**

FIG. 1. Simplified tectonic map of eastern Tibetan Plateau (modified after Campbell et al. 2014; Leloup et al. 1995).

FIG. 2. The minerals assemblage of the Yulong porphyry, Duoxiasongduon porphyry, and Zhanaga porphyry. Abbreviation: Amp=amphibole, Bio=biotite, Kfs=K-feldspar, Pla=plagioclase, and Qtz=quartz.

FIG. 3. Representative photos of (A) CL image showing the zircon structure, and (B) primary fluid inclusions in zircon from fertile porphyries under transmitted light.

FIG. 4. Backscattered-electron (BSE) of represent apatites with different occurrences. (A) apatite inclusion within plagioclase phenocryst, (B) the apatite inclusions within the biotite phenocrysts, (C) the apatite inclusions host by altered amphibole, with (D) zoning texture showing primary and magmatic origin, (E) apatite inclusion host by quartz with (F) zoning texture showing primary and magmatic origin, (G) apatite in groundmass with (H) zoning texture showing primary and magmatic origin.

FIG. 5. Bulk-rock (A) total alkaline (TAS), and (B) the K_2O vs. SiO_2 diagrams of the samples.

FIG. 6. Primitive mantle normalized bulk rock trace element and chondrite-normalized bulk rock rare earth elements (REEs) patterns for Yulong porphyry (A, B), Duoxiasongduo porphyry (C, D) and Zhanaga porphyry (E, F). The normalized values are from Sun and McDonough (1989). Legends are the same as those in Fig. 5.

FIG. 7. The zircon $\delta^{18}O$ vs. $\varepsilon_{Hf}(t)$. Solid lines are isotopic mixing curves, and the open circles along lines denote 10% intervals. Hf_m/Hf_c is the ratio of Hf concentration in the

mantle (m) and the crust (c). Identical oxygen contents (50%) in the mantle and crust were assumed. Depleted mantle source has $\varepsilon_{Hf}(t)$=+17 and $\delta^{18}O$=+5.3‰; Continental crust has $\varepsilon_{Hf}(t)$=-35, $\delta^{18}O$ =+ 9.5‰. The composition of continental crustal zircon $\delta^{18}O$ was from Yang et al. (2021). Legends are the same as those in Fig. 5.

FIG. 8. The average chondrite-normalized zircon REE patterns. Legends are the same as those in Fig. 5.

FIG. 9. Plots of REE+Y vs. P (A and B), and vs. P+H_2O_{total} (C and D).

FIG. 10. Zircon H_2O contents in ppm (A), calculated maximum H^+ content (B), and the (C) calculated minimum OH^- contents vs. the mineralization size of the porphyry deposits. Legends are the same as those in Fig. 9.

FIG. 11. Plots of (A) calculated maximum H^+ vs. H_2O_{total}, (B) calculated minimum OH^- vs. H_2O_{total}, and (C) maximum calculated H^+ vs. minimum OH^-. Legends are the same as those in Fig. 9.

FIG. 12. The Cl contents vs. F contents, and SO_3 content vs. SiO_2 contents of the apatite from the Yulong porphyry (A, D), the Duoxiasongduo porphyry (B, E) and the Zhanaga porphyry (C, F).

FIG. 13. Scatter plots of apatite compositions in X_{Cl}^{Ap}/X_{OH}^{Ap} vs. X_F^{Ap}/X_{Cl}^{Ap} of (A) Yulong, (B) Duxiasongduo, and (C) Zhanaga porphyry deposits. The same data are also shown according to apatite textural associations, including zircon-hosted (D), phenocryst-hosted (E), and in groundmass (F).

FIG. 14. (A) Schematic diagram summarizing the water content evolution of porphyry magmas that formed medium-size deposit (B) and giant/large deposit (C), and their relations with the depth-dependent water solubility (blue solid line).

Table

TABLE 1 Summarized the volatile compositions of apatite with different occurrences from the three studied porphyry deposits in YCB

Appendix

FIG. A1. Representative $\nu_3(SiO_4)$ Raman band of zircon grains from the three intrusions.

FIG. A2. Chondrite-normalized REE patterns of each zircon grain.

FIG. A3. Variations between zircon (A) Mg, (B) Fe, and (C) Al contents and the REE+Y contents. Values are given as atoms per functional zircon unit based on 4 oxygen (apfu.) multiplied by 1000.

FIG. A4. Scatter plots of apatite compositions in X_{Cl}^{Ap}/X_{OH}^{Ap} vs. X_{F}^{Ap}/X_{OH}^{Ap} of (A) Yulong, (B) Duxiasongduo, and (C) Zhanaga porphyry deposits. The same data are also shown according to apatite textural associations, including zircon-hosted (D), phenocryst-hosted (E), and in groundmass (F).

TABLE A1. Whole rock major and trace element composition of the three porphyries from YCB

TABLE A2. Laser Raman spectra and LA-ICP-MS trace element composition (in ppm) concentrations of the zircons from three porphyries from eastern Tibet

1017 **TABLE A3.** Water content and O isotopic composition of zircon from three porphyries

1018 from eastern Tibet by SIMS

1019 **TABLE A4.** Hf isotopic composition of zircon from the three porphyries from eastern

1020 Tibet by MC LA-ICP-MS

1021 **TABLE A5.** Major and volatile element composition of zircon-hosted, phenocryst-host

1022 and groundmass apatites from the three porphyries in YCB

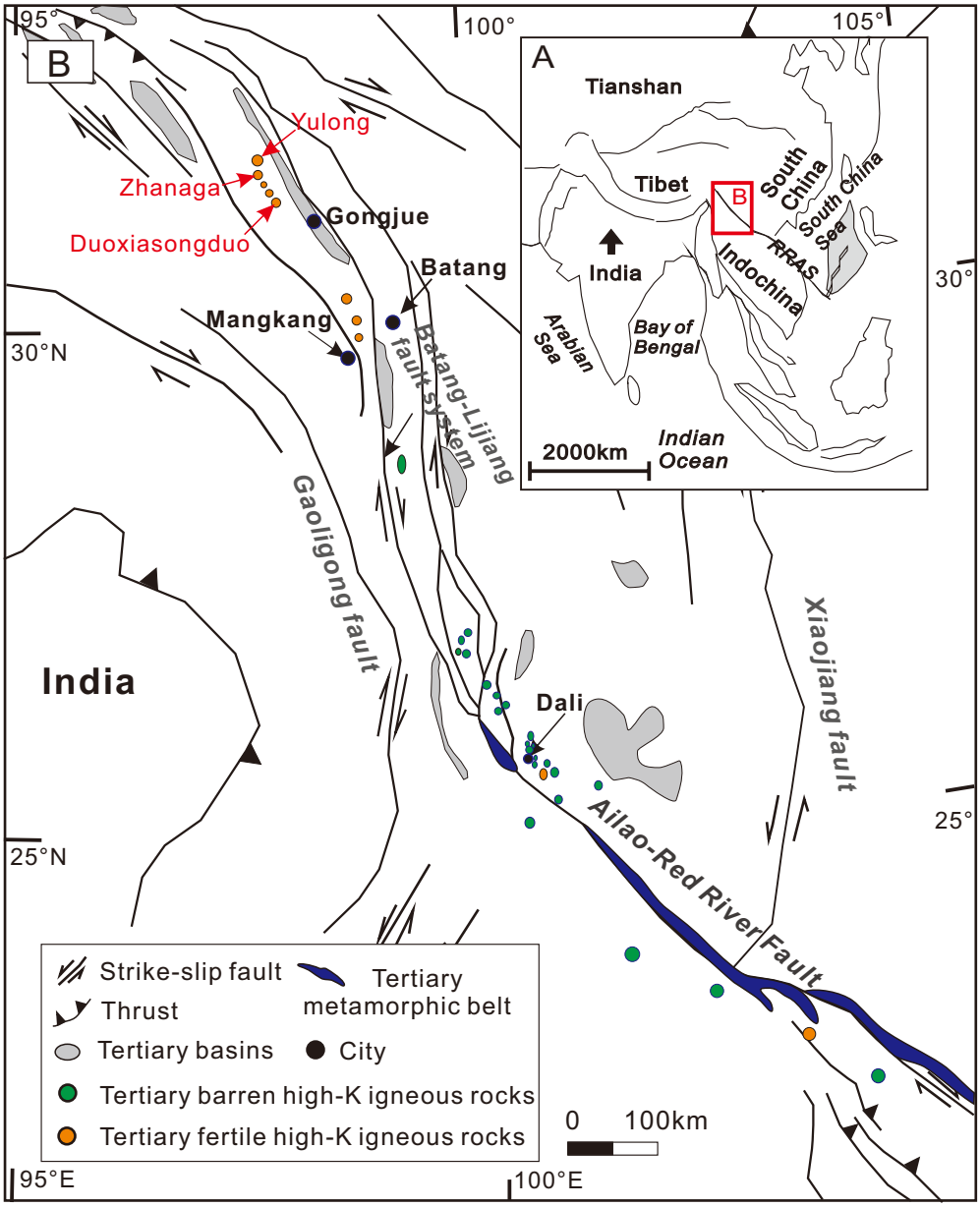
95°
100°
105°
B
A
Tianshan
Tibet
B
South China
South China Sea
India
Indochina
RRAS
Arabian Sea
Bay of Bengal
2000km
Indian Ocean
30°
Yulong
Zhanaga
Duoxiasongduo
Gongjue
Batang
Mangkang
30°N
Batang-Lijiang fault system
Gaoligong fault
India
Dali
Xiaojiang fault
Ailao-Red River Fault
25°
25°N
Strike-slip fault
Thrust
Tertiary basins
Tertiary barren high-K igneous rocks
Tertiary fertile high-K igneous rocks
Tertiary metamorphic belt
City
0
100km
95°E
100°E

Fig. 1

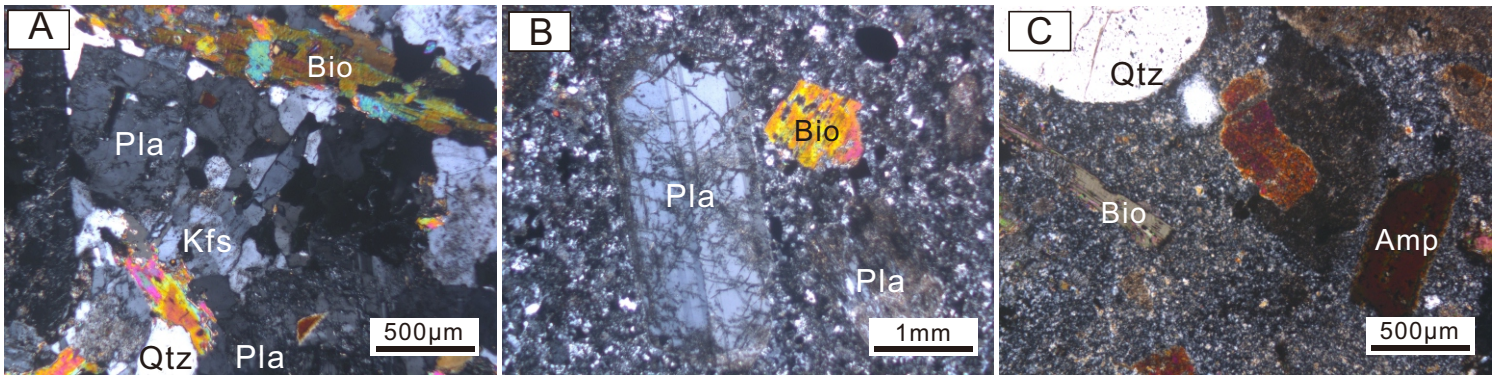

Fig.2

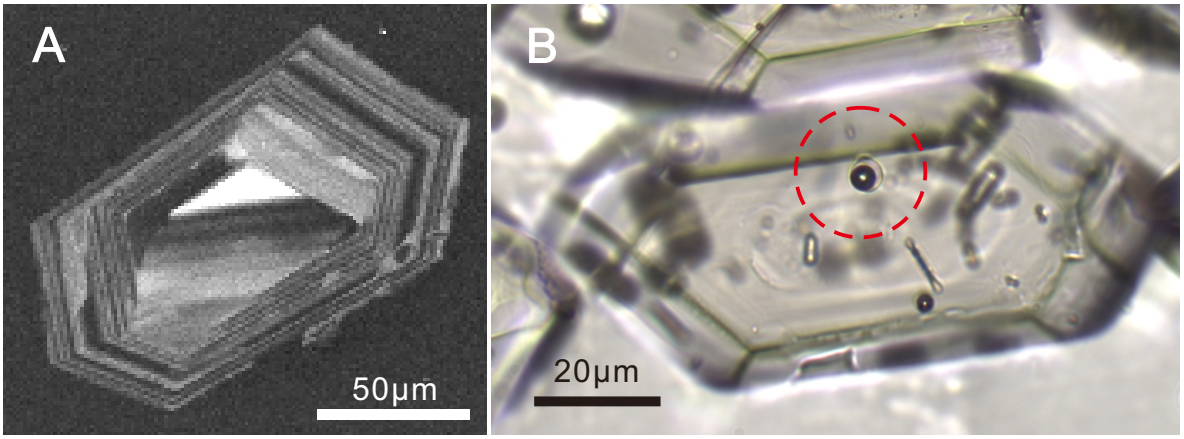

Fig.3

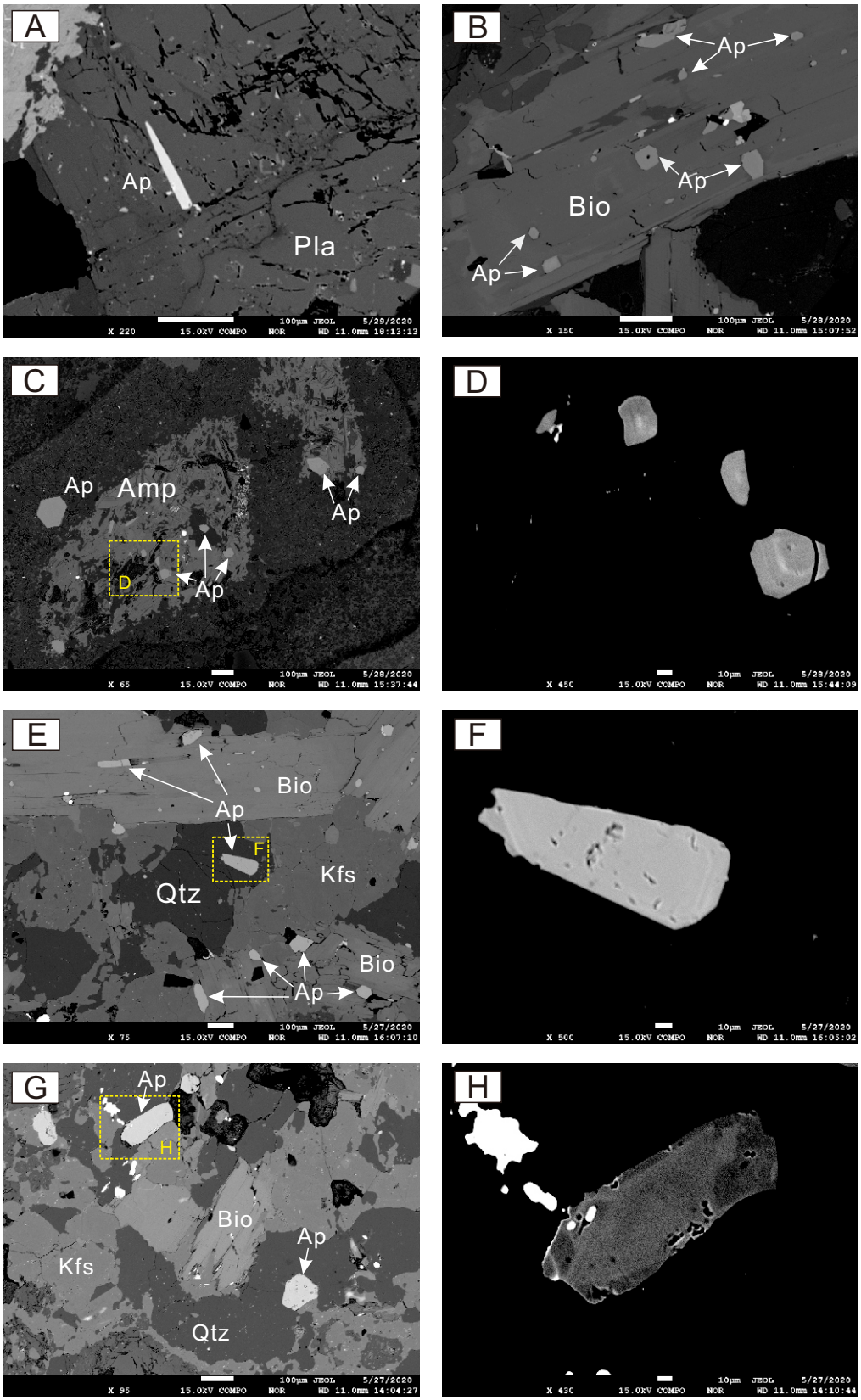
A
Ap
Pla
B
Ap
Ap
Bio
Ap
C
Ap
Amp
Ap
D
Ap
D
E
Bio
Ap
F
Kfs
Qtz
Bio
Ap
F
G
Ap
H
Bio
Ap
Kfs
Qtz
H

Fig.4

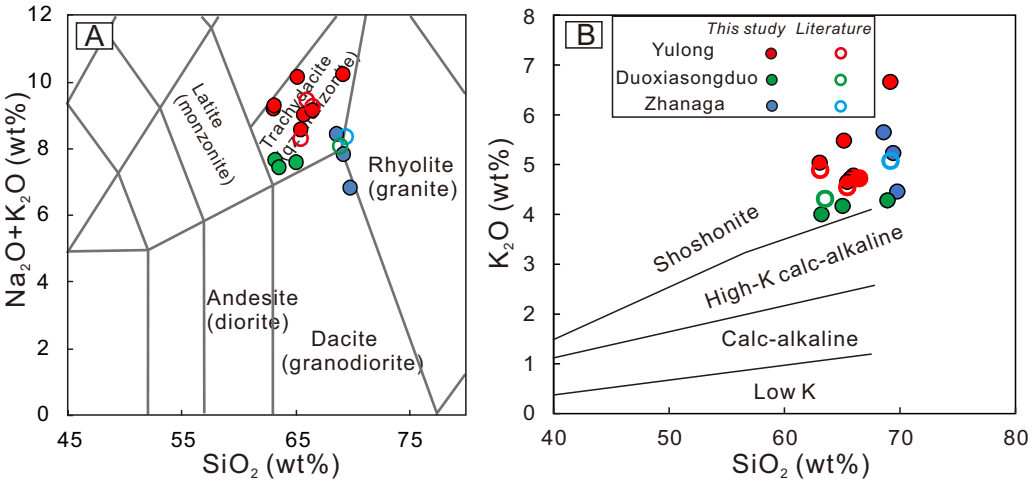
A
Latite
(monzonite)
Trachydacite
(quartz monzonite)
Rhyolite
(granite)
Andesite
(diorite)
Dacite
(granodiorite)
Na2O+K2O (wt%)
SiO2 (wt%)
B
This study Literature
Yulong
Duoxiasongduo
Zhanaga
Shoshonite
High-K calc-alkaline
Calc-alkaline
Low K
K2O (wt%)
SiO2 (wt%)

Fig. 5

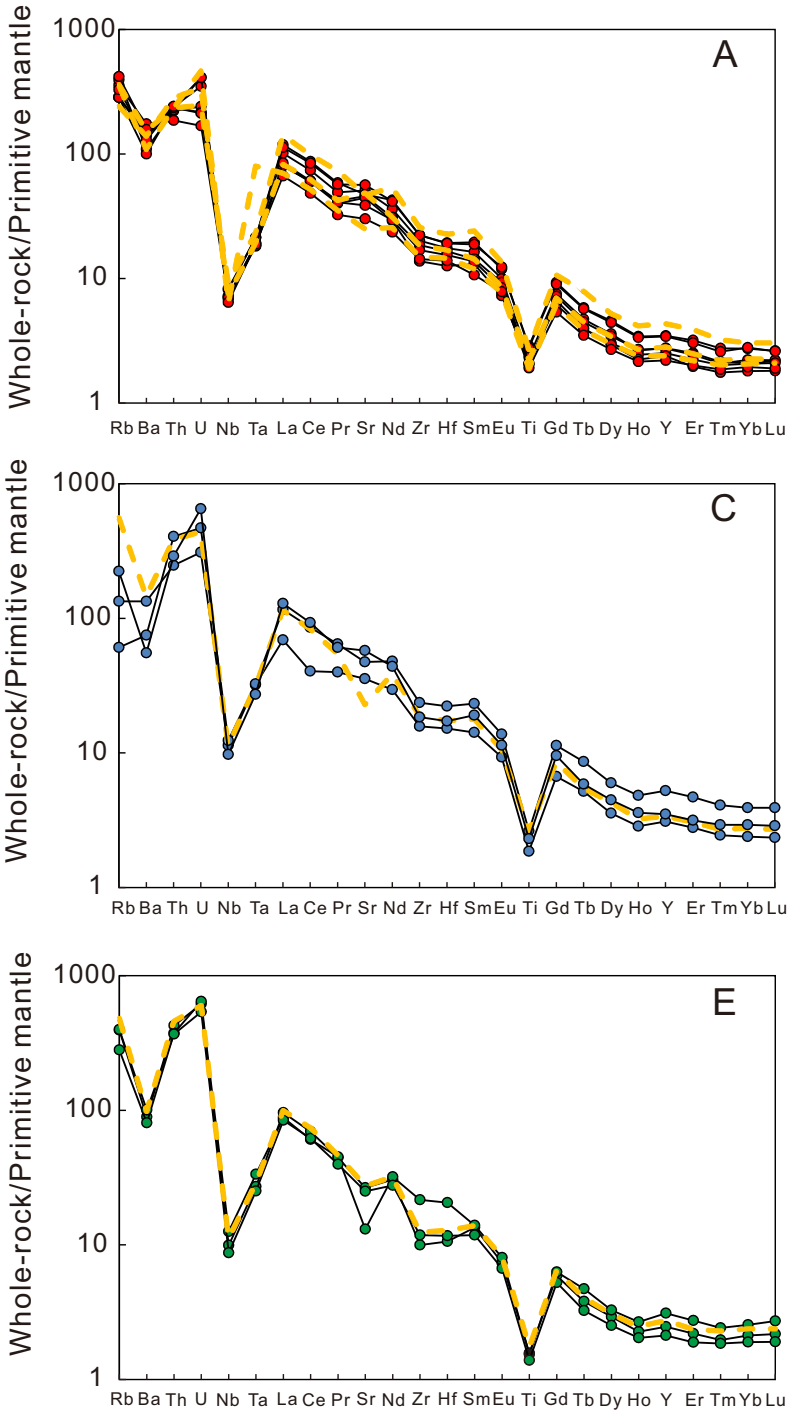
A
B
C
D
E
F
Whole-rock/Primitive mantle
Whole-rock/Chondrite
1000
100
10
1
Rb Ba Th U Nb Ta La Ce Pr Sr Nd Zr Hf Sm Eu Ti Gd Tb Dy Ho Y Er Tm Yb Lu
La Ce Pr Nd Sm Eu Gd Tb Dy Ho Er Tm Yb Lu

Fig. 6

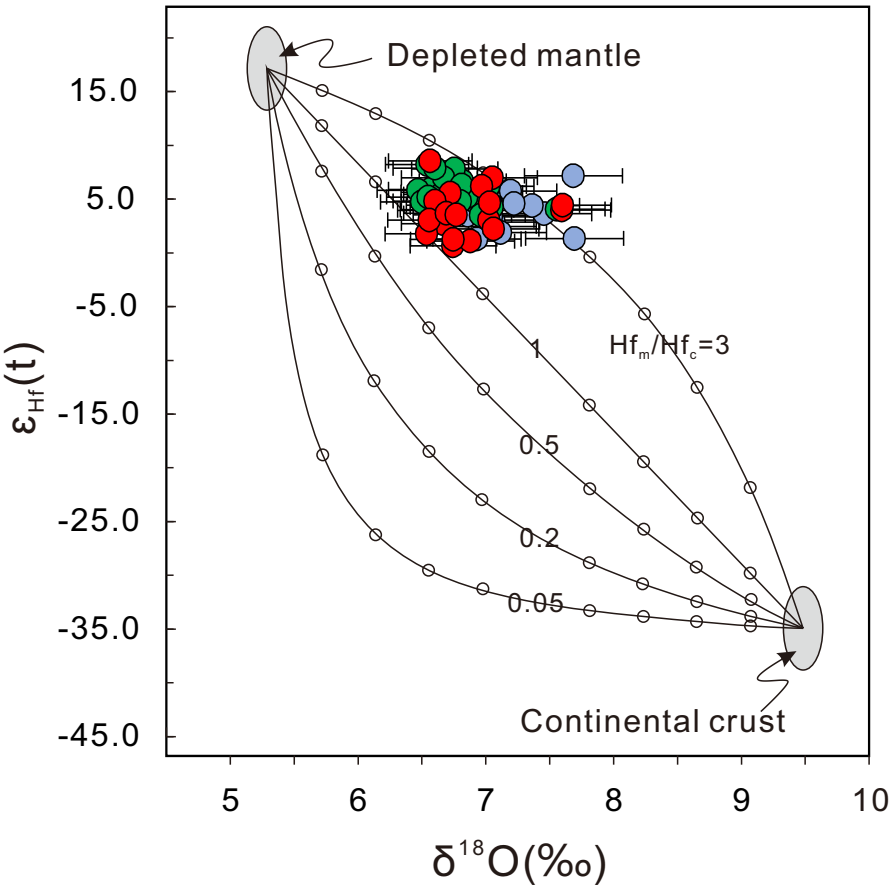
Depleted mantle
15.0
5.0
-5.0
-15.0
-25.0
-35.0
-45.0
$\varepsilon_{Hf}(t)$
1
Hf_m/Hf_c=3
0.5
0.2
0.05
Continental crust
5
6
7
8
9
10
$\delta^{18}O(‰)$

Fig. 7

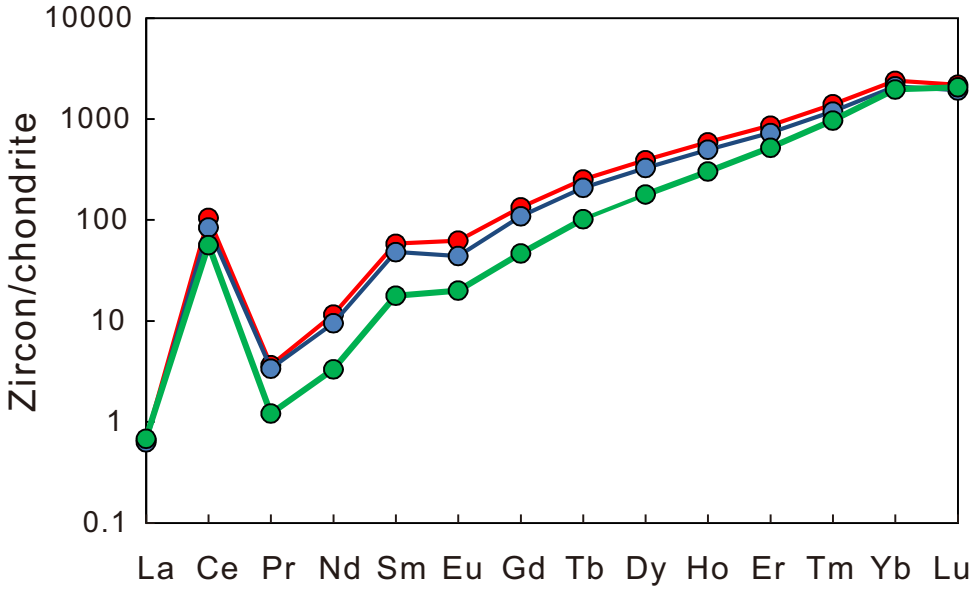
10000
1000
100
10
1
0.1
Zircon/chondrite
La Ce Pr Nd Sm Eu Gd Tb Dy Ho Er Tm Yb Lu

Fig. 8

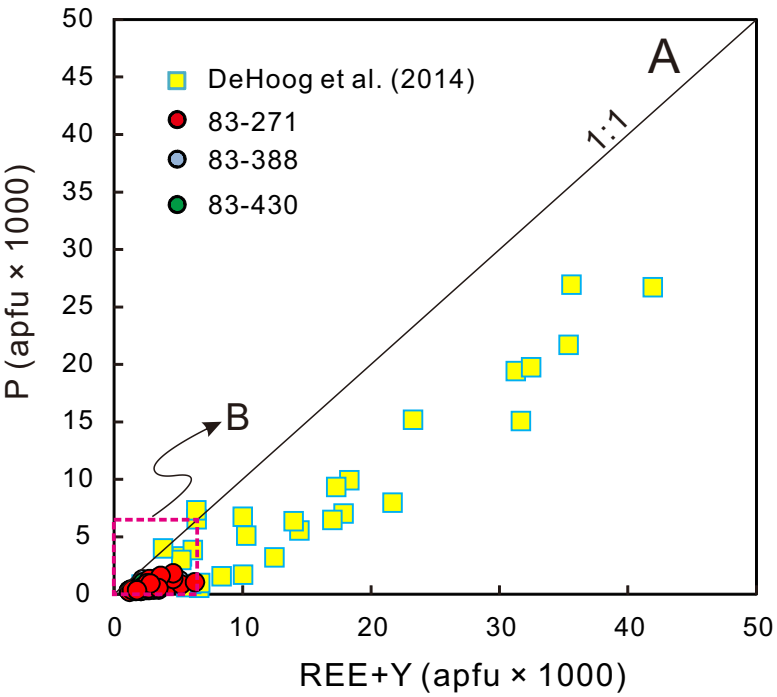
A
DeHoog et al. (2014)
83-271
83-388
83-430
1:1
B
P (apfu × 1000)
REE+Y (apfu × 1000)

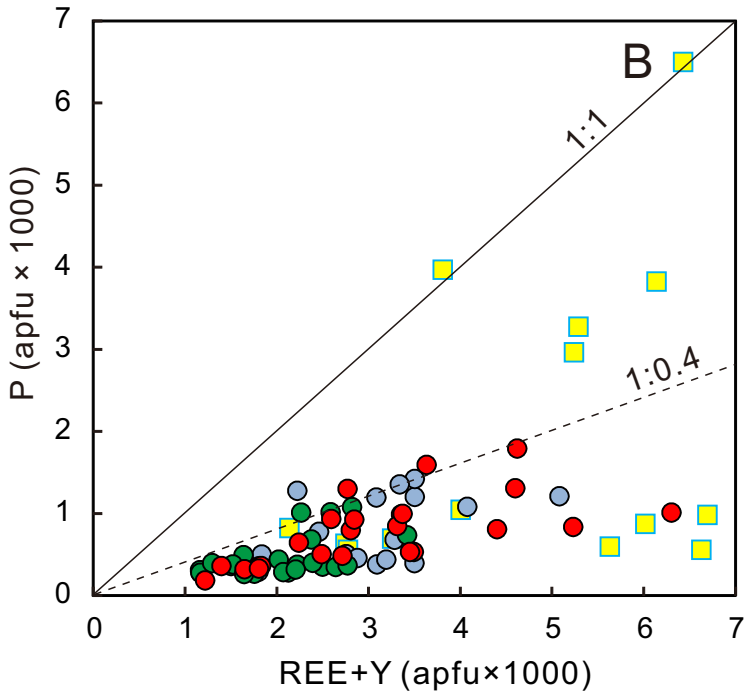
B
1:1
1:0.4
P (apfu × 1000)
REE+Y (apfu×1000)

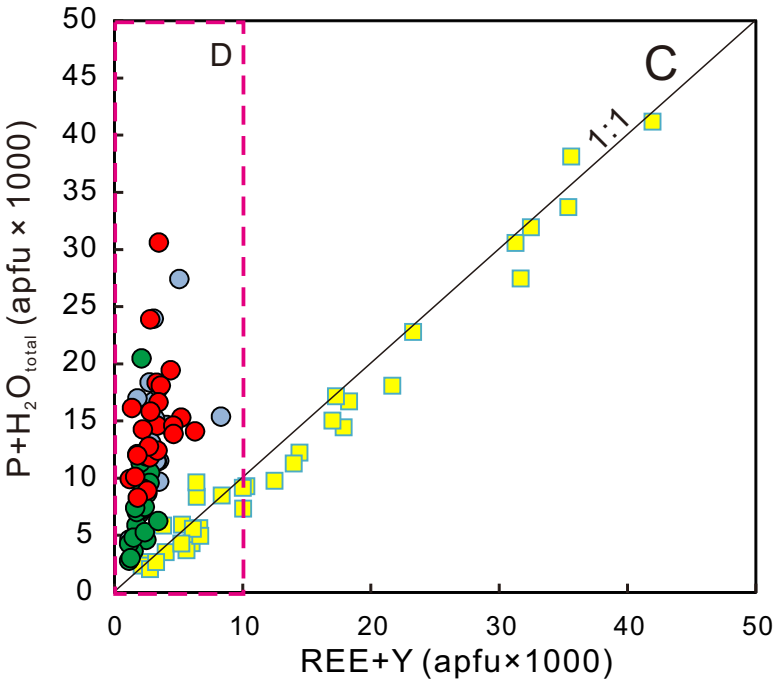
D
C
1:1
P+H2Ototal (apfu × 1000)
REE+Y (apfu×1000)

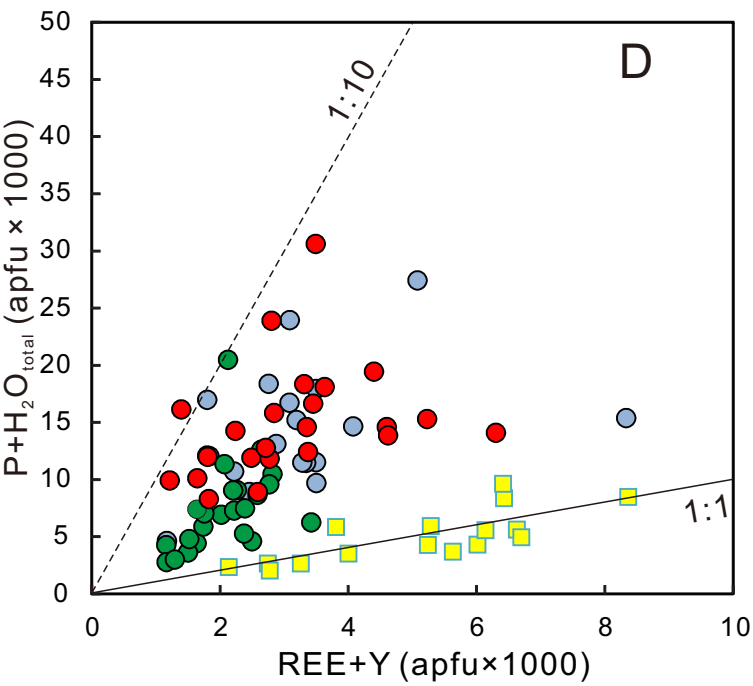
D
1:10
1:1
P+H2Ototal (apfu × 1000)
REE+Y (apfu×1000)

Fig.9

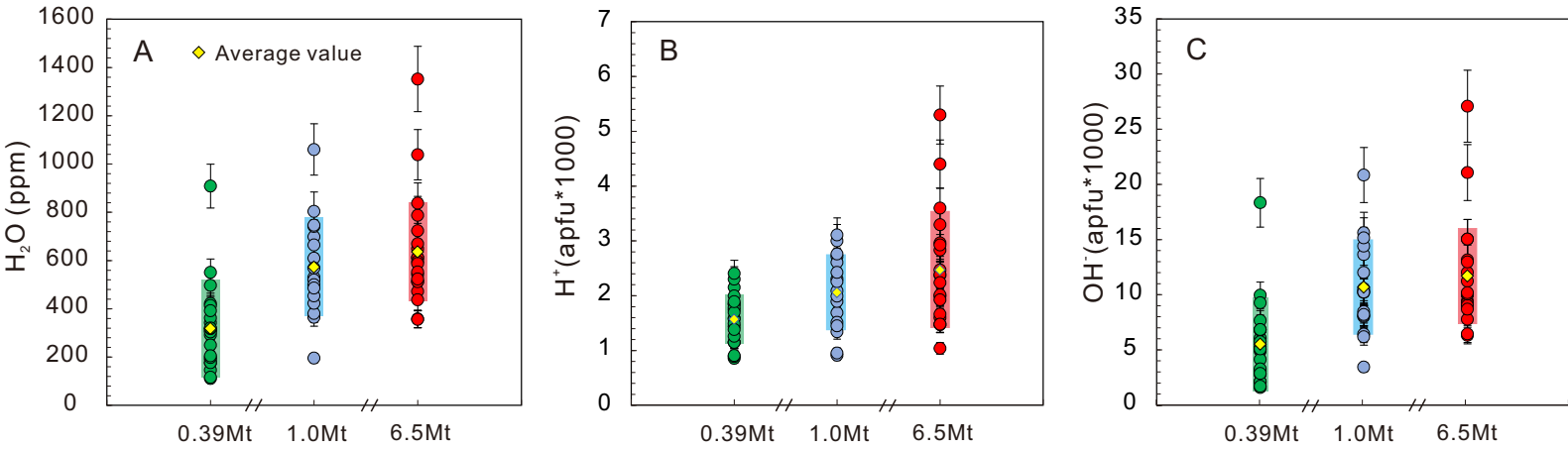
A
Average value
H_2O (ppm)
1600
1400
1200
1000
800
600
400
200
0
0.39Mt
1.0Mt
6.5Mt
B
H^+(apfu*1000)
7
6
5
4
3
2
1
0
0.39Mt
1.0Mt
6.5Mt
C
OH^-(apfu*1000)
35
30
25
20
15
10
5
0
0.39Mt
1.0Mt
6.5Mt

Fig.10

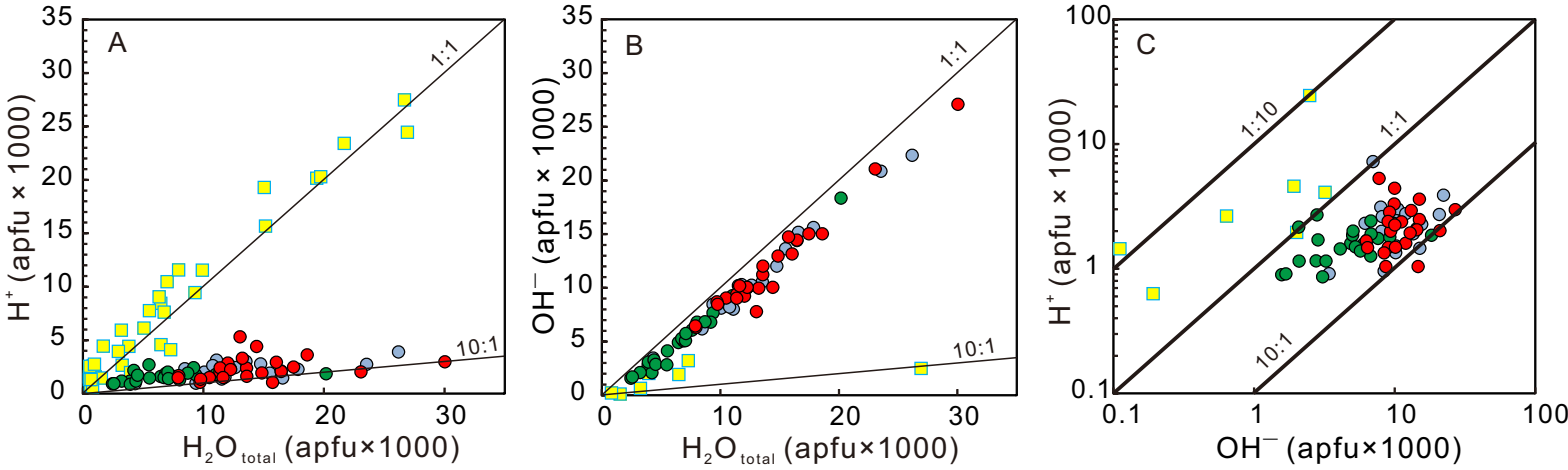
A
B
C
1:1
10:1
1:10
H+ (apfu × 1000)
OH− (apfu × 1000)
H2Ototal (apfu×1000)
OH− (apfu×1000)

Fig. 11

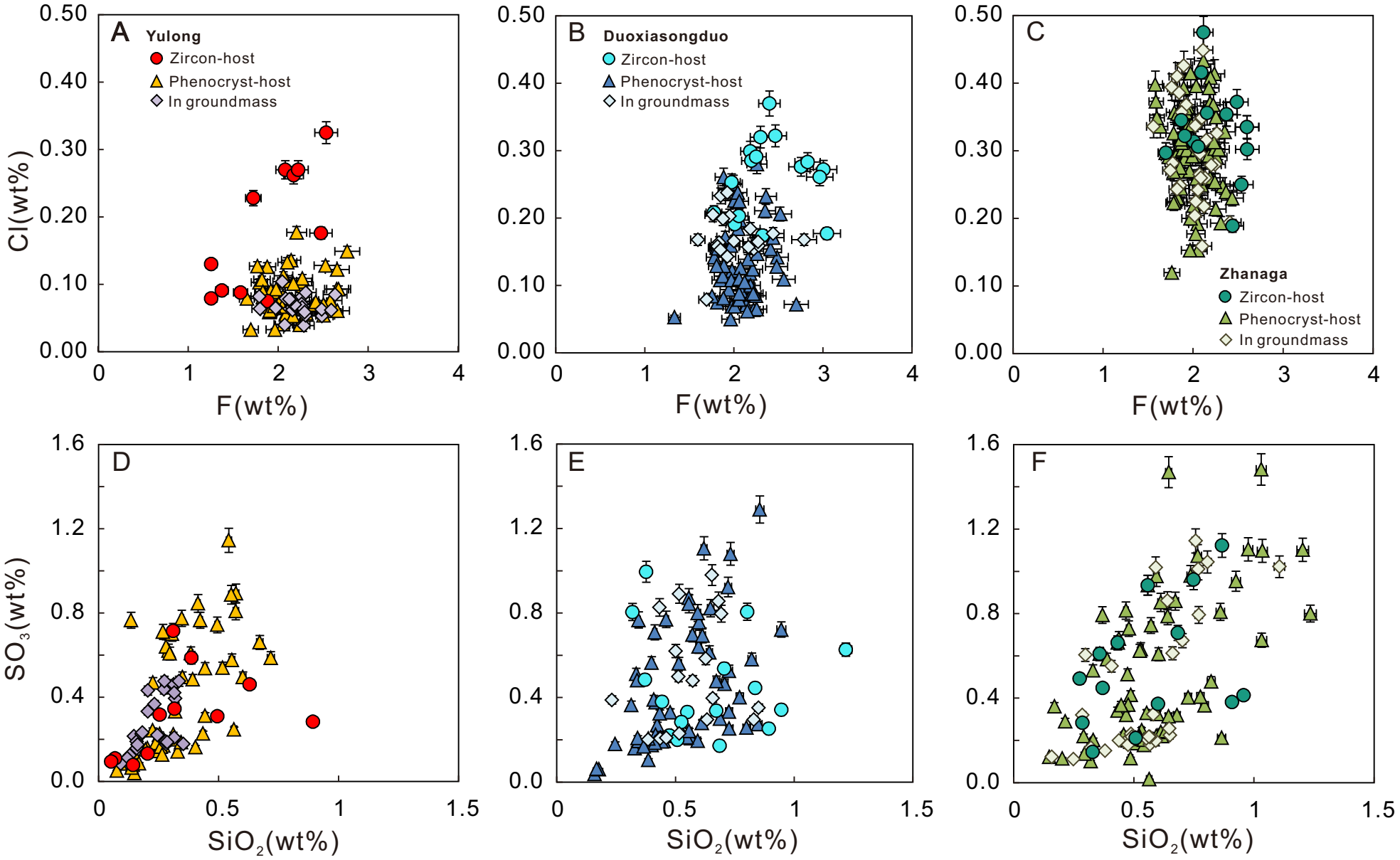
A
Yulong
Zircon-host
Phenocryst-host
In groundmass
B
Duoxiasongduo
Zircon-host
Phenocryst-host
In groundmass
C
Zhanaga
Zircon-host
Phenocryst-host
In groundmass
Cl(wt%)
F(wt%)
D
E
F
SO3(wt%)
SiO2(wt%)

Fig. 12

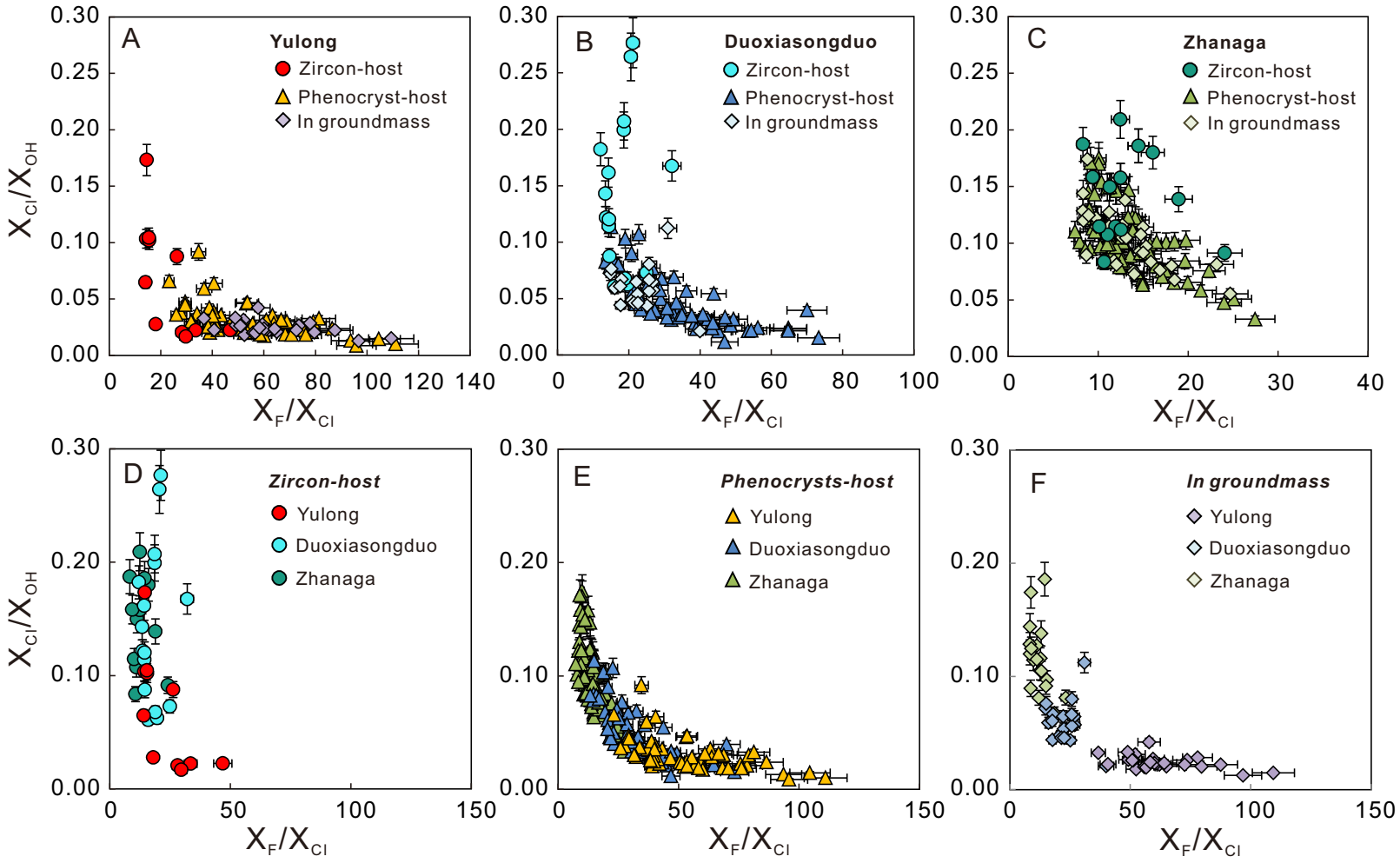
A
Yulong
Zircon-host
Phenocryst-host
In groundmass
B
Duoxiasongduo
Zircon-host
Phenocryst-host
In groundmass
C
Zhanaga
Zircon-host
Phenocryst-host
In groundmass
D
Zircon-host
Yulong
Duoxiasongduo
Zhanaga
E
Phenocrysts-host
Yulong
Duoxiasongduo
Zhanaga
F
In groundmass
Yulong
Duoxiasongduo
Zhanaga
X_{Cl}/X_{OH}
X_F/X_{Cl}

Fig. 13

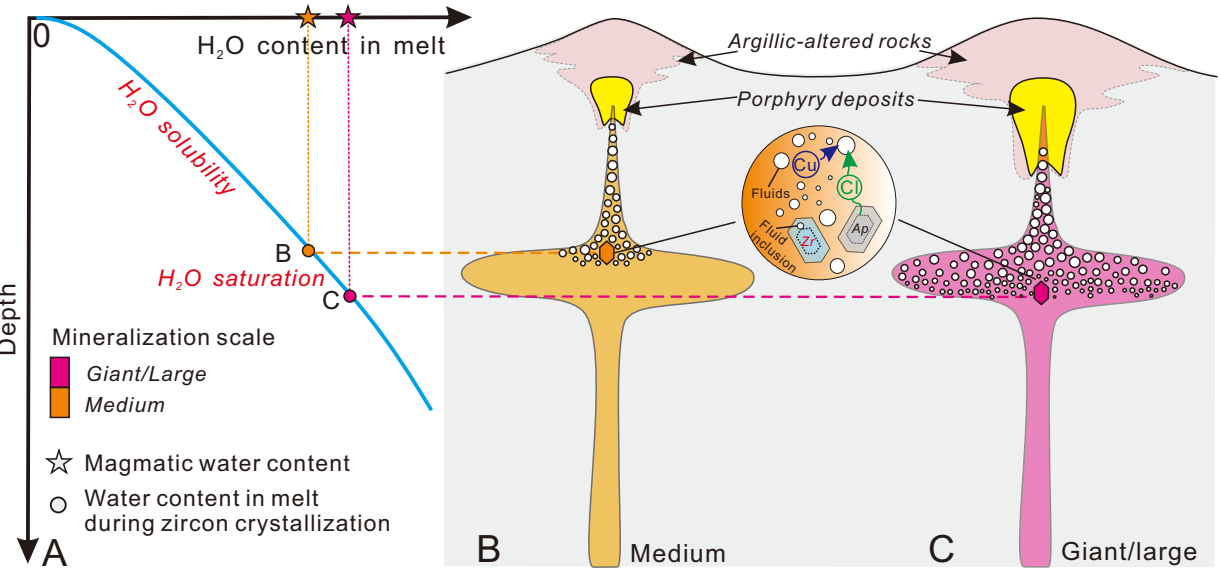
0
H2O content in melt
H2O solubility
B
H2O saturation
C
Depth
A
Mineralization scale
Giant/Large
Medium
Magmatic water content
Water content in melt
during zircon crystallization
Argillic-altered rocks
Porphyry deposits
Cu
Cl
Fluids
Fluid inclusion
Zr
Ap
B
Medium
C
Giant/large

Fig. 14

Table 1 Summarized the volatile compositions of apatite with different occurrences from the three studied porphyry deposits in YCB

Apatite occurrences	Compositions	Phenocryst host				Groundmass	Zircon host
		Biotite	Plagioclase	Quartz	Amphibole		
Yulong giant porphyry deposit	*n*	*16*	*15*	*23*		*25*	*11*
	Cl(wt.%)	0.03-0.11	0.06-0.18	0.03-0.13		0.04-0.10	0.08-0.33
	F(wt.%)	1.65-2.65	1.88-2.77	1.77-2.66		1.79-2.63	1.26-2.54
	SO_3(wt.%)	0.22-1.14	0.08-0.89	0.04-0.77		0.08-0.48	0.08-0.71
	X_{Cl}/X_{OH}	0.01-0.05	0.02-0.09	0.01-0.06		0.01-0.04	0.02-0.17
	X_F/X_{Cl}	39.0-104	23.3-79.2	26.0-111		36.7-109	14.1-46.9
	X_F/X_{OH}	0.79-2.52	1.05-3.18	0.93-2.65		0.92-2.43	0.50-2.52
Duoxiasongduo large porphyry deposit	*n*	*19*	*25*	*22*	*16*	*19*	*16*
	Cl(wt.%)	0.07-0.21	0.06-0.28	0.19-0.43	0.05-0.15	0.08-0.24	0.17-0.37
	F(wt.%)	1.78-2.70	1.83-2.48	1.86-2.37	1.33-2.49	1.60-2.79	1.78-3.05
	SO_3(wt.%)	0.06-1.29	0.06-1.08	0.02-1.47	0.04-1.11	0.20-0.98	0.17-1.00
	X_{Cl}/X_{OH}	0.03-0.11	0.02-0.11	0.07-0.18	0.01-0.07	0.02-0.11	0.06-0.28
	X_F/X_{Cl}	20.6-70.0	13.5-64.8	9.13-22.3	29.2-73.3	14.8-40.0	12.1-33.1
	X_F/X_{OH}	0.93-2.77	1.00-2.05	1.06-1.87	0.54-2.25	0.78-3.48	0.97-5.86
Zhanaga medium porphyry deposit	*n*	*22*	*21*	*11*	*33*	*19*	*14*
	Cl(wt.%)	0.19-0.43	0.15-0.40	0.16-0.37	0.12-0.42	0.19-0.45	0.19-0.48
	F(wt.%)	1.86-2.37	1.58-2.44	1.78-2.25	1.64-2.37	1.56-2.60	1.70-2.60
	SO_3(wt.%)	0.02-1.47	0.11-1.10	0.11-1.04	0.10-1.48	0.18-1.14	0.15-1.12
	X_{Cl}/X_{OH}	0.07-0.18	0.05-0.12	0.06-0.12	0.03-0.16	0.07-0.19	0.08-0.21
	X_F/X_{Cl}	9.13-22.3	7.42-25.1	9.76-24.7	8.57-27.4	8.30-23.2	8.31-24.1
	X_F/X_{OH}	1.06-1.87	0.80-2.03	0.99-1.71	0.86-1.97	0.78-2.69	0.89-2.89

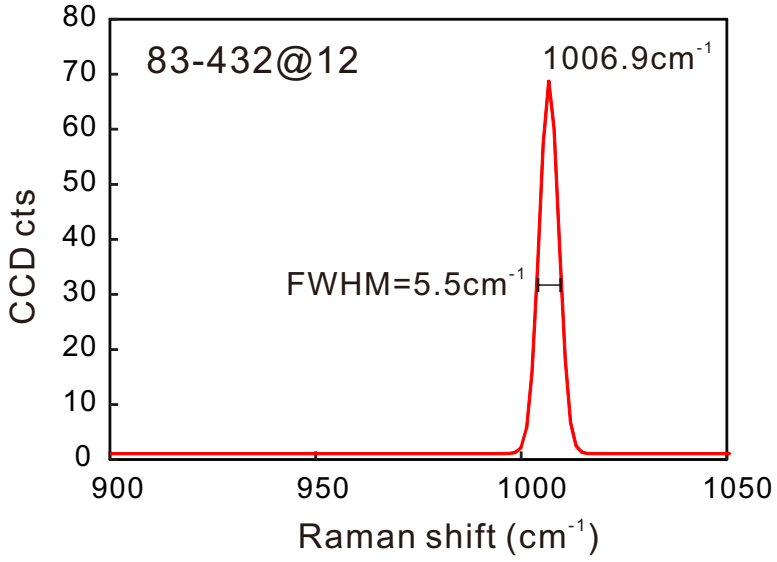
83-432@12
1006.9cm-1
FWHM=5.5cm-1
CCD cts
Raman shift (cm-1)
0
10
20
30
40
50
60
70
80
900
950
1000
1050

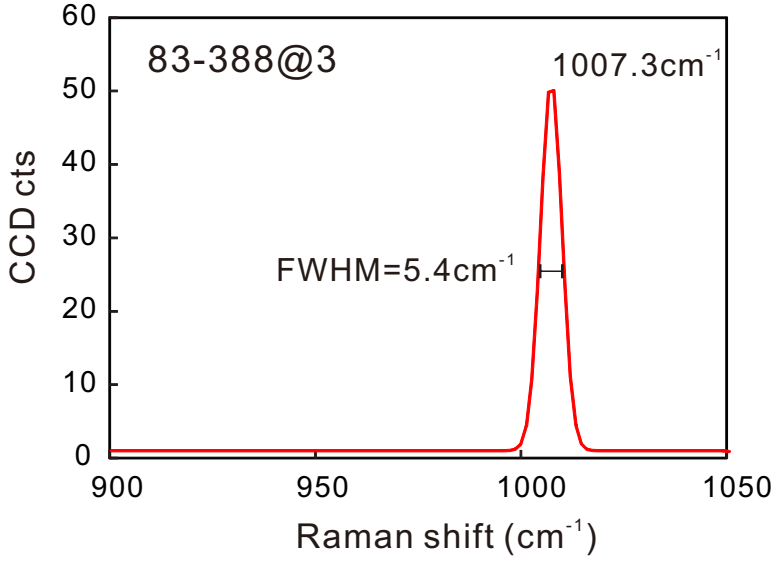
83-388@3
1007.3cm-1
FWHM=5.4cm-1
CCD cts
Raman shift (cm-1)
0
10
20
30
40
50
60
900
950
1000
1050

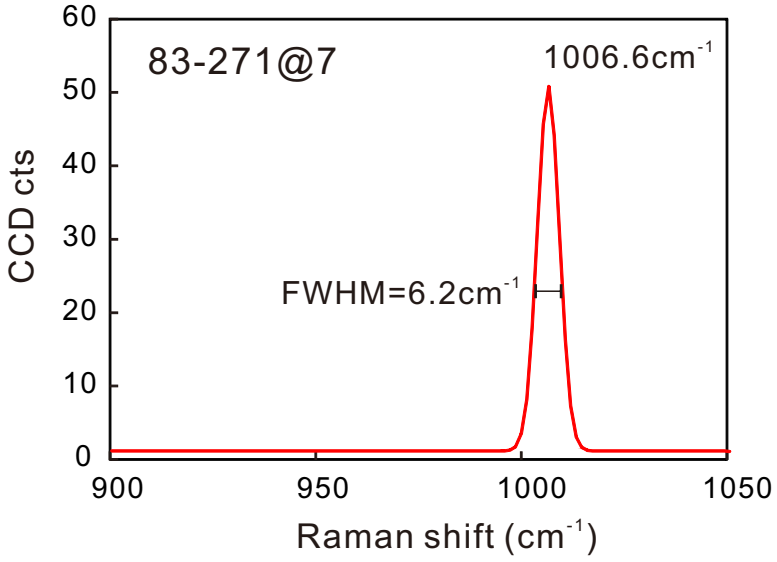
83-271@7
1006.6cm-1
FWHM=6.2cm-1
CCD cts
Raman shift (cm-1)
0
10
20
30
40
50
60
900
950
1000
1050

Fig. A1

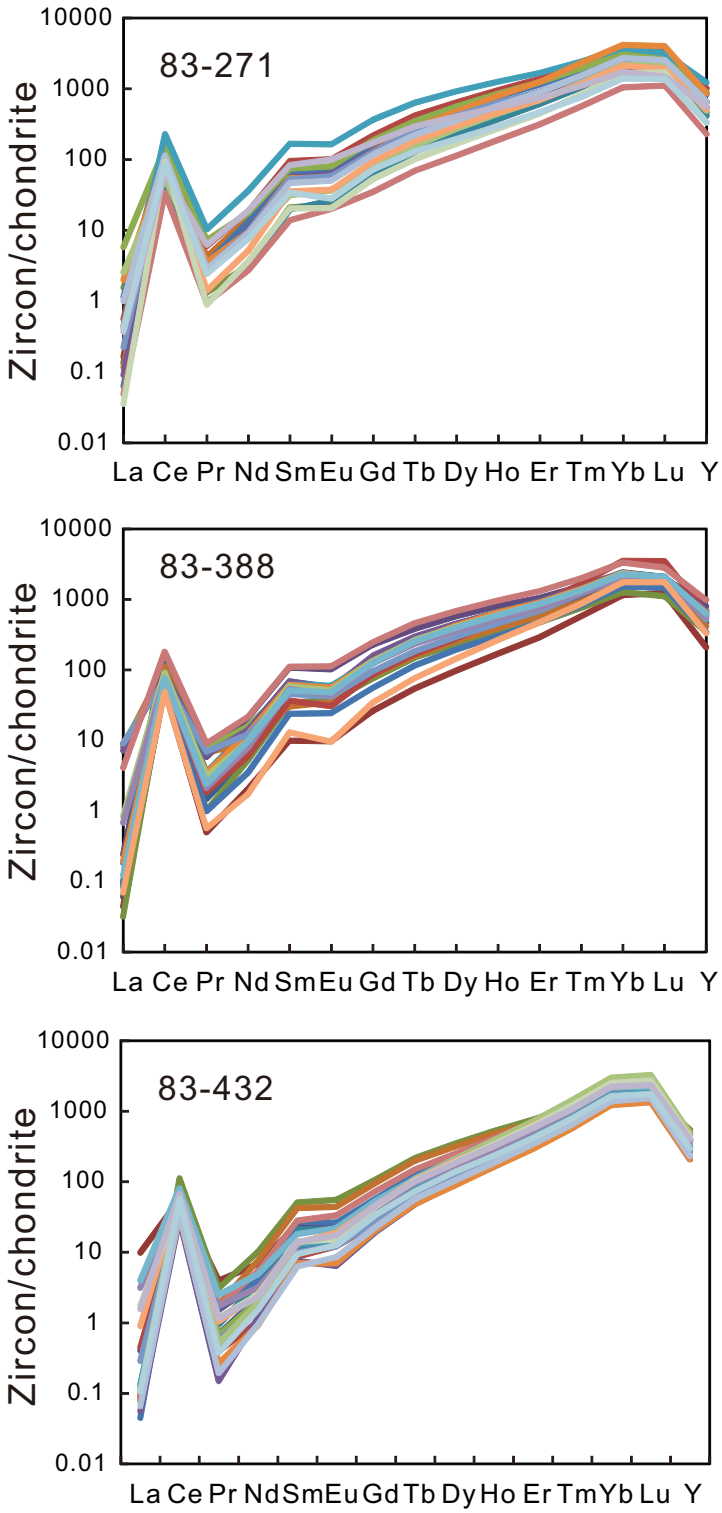
83-271
83-388
83-432
Zircon/chondrite
10000
1000
100
10
1
0.1
0.01
La Ce Pr Nd Sm Eu Gd Tb Dy Ho Er Tm Yb Lu Y

Fig. A2

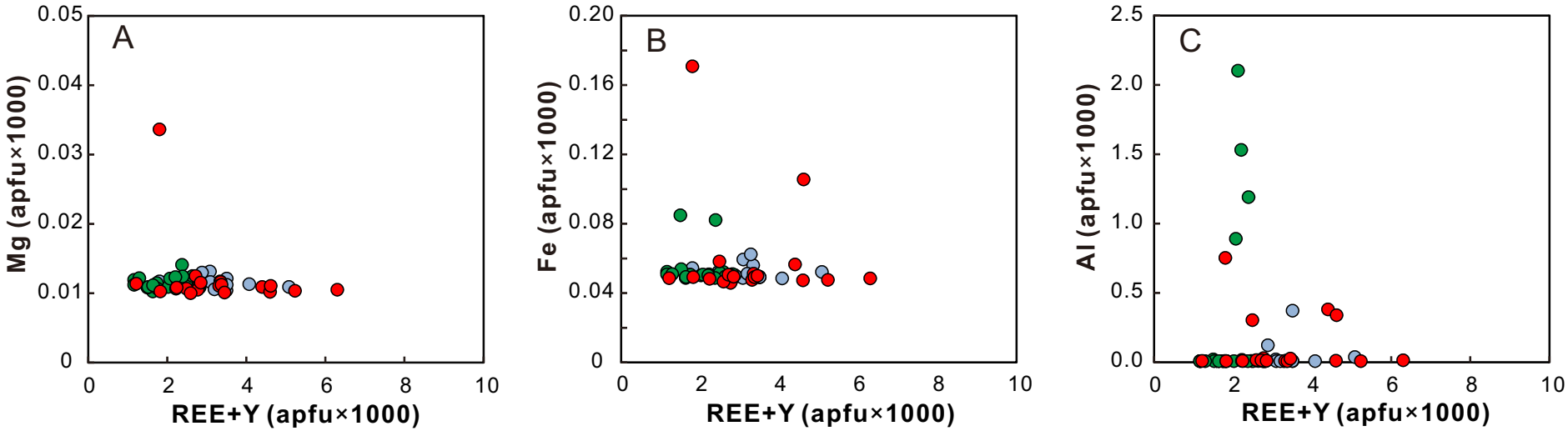
A
B
C
Mg (apfu×1000)
Fe (apfu×1000)
Al (apfu×1000)
REE+Y (apfu×1000)
REE+Y (apfu×1000)
REE+Y (apfu×1000)
0.05
0.04
0.03
0.02
0.01
0
0.20
0.16
0.12
0.08
0.04
2.5
2.0
1.5
1.0
0.5
0.0
0
2
4
6
8
10

Fig. A3

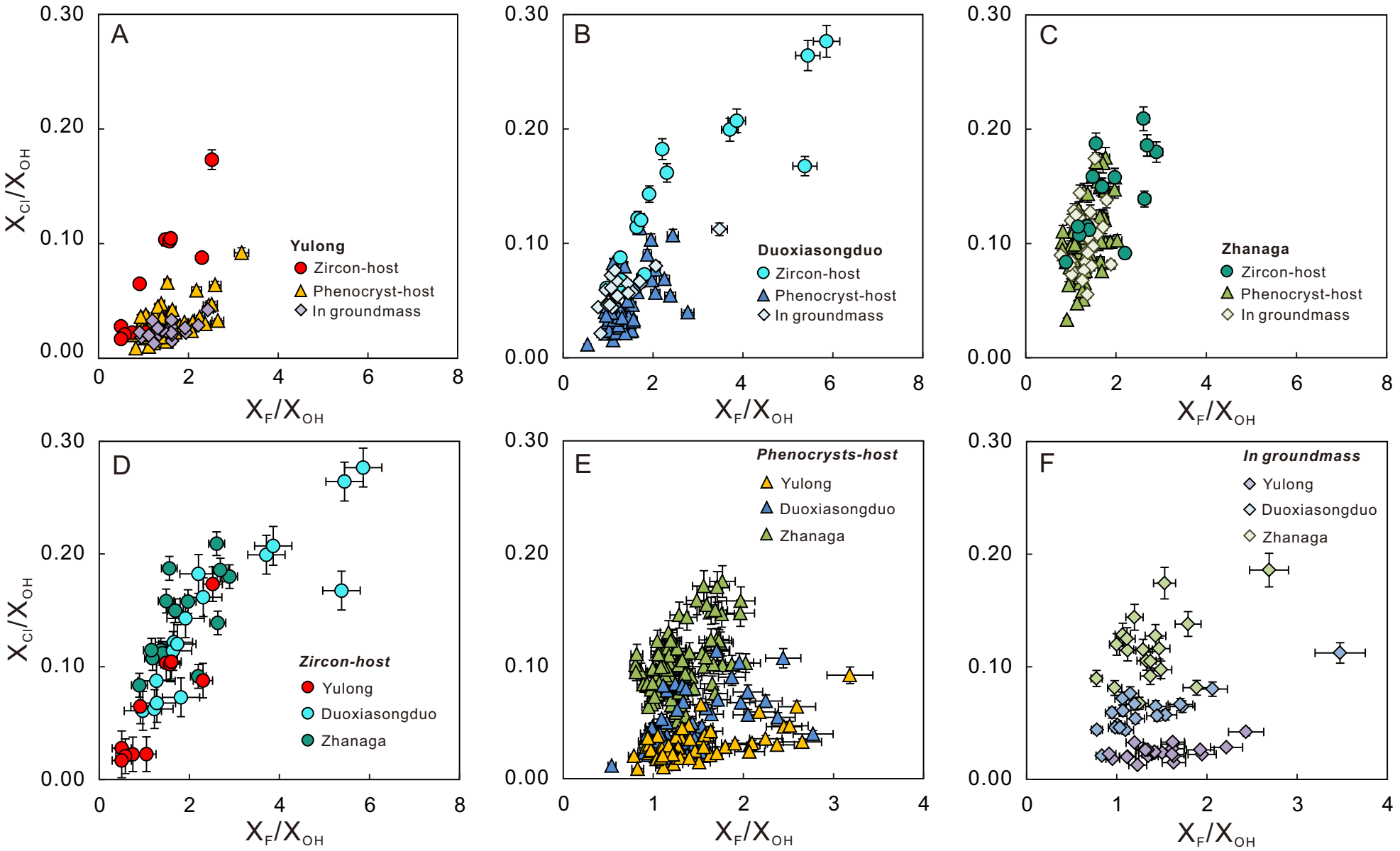
A
Yulong
Zircon-host
Phenocryst-host
In groundmass
B
Duoxiasongduo
Zircon-host
Phenocryst-host
In groundmass
C
Zhanaga
Zircon-host
Phenocryst-host
In groundmass
D
Zircon-host
Yulong
Duoxiasongduo
Zhanaga
E
Phenocrysts-host
Yulong
Duoxiasongduo
Zhanaga
F
In groundmass
Yulong
Duoxiasongduo
Zhanaga
X_{Cl}/X_{OH}
X_F/X_{OH}

Fig. A4